SAND2023-05008J

Exploring pressure-dependent inelastic deformation and failure in bonded granular composites: an energetic materials perspective

Joel T. Clemmer[a], Kevin N. Long[a], Judith A. Brown[a,*]

[a]*Engineering Sciences Center, Sandia National Laboratories, Albuquerque, New Mexico, 87185, USA*

Abstract

In polymer-filled granular composites, damage may develop in mechanical loading prior to material failure. Damage mechanisms such as microcracking or plastic deformation in the binder phase can substantially alter the material's mesostructure. For energetic materials, such as solid propellants and plastic bonded explosives, these mesostructural changes can have far reaching effects including degraded mechanical properties, potentially increased sensitivity to further insults, and changes in expected performance. Unfortunately, predicting damage is nontrivial due to the complex nature of these composites and the entangled interactions between inelastic mechanisms. In this work, we assess the current literature of experimental knowledge, focusing on the pressure-dependent shear response, and propose a simple simulation framework of bonded particles to study four limiting-case material formulations at both meso- and macro-scales. To construct the four cases, we systematically vary the relative interfacial strength between the polymer binder and granular filler phase and also vary the polymer's glass transition temperature relative to operating temperature which determines how much the binder can plastically deform. These simulations identify key trends in global mechanical response, such as the emergence of strain hardening or softening regimes with increasing pressure which qualitatively resemble experimental results. By quantifying the activation of different inelastic mechanisms, such as bonds breaking and plastically straining, we identify when each mechanism becomes relevant and provide insight into potential origins for changes in mechanical responses. The locations of broken bonds are also used to define larger, mesoscopic cracks to test various metrics of damage. We primarily focus on triaxial compression, but also test the opposite case of triaxial extension to highlight the impact of Lode angle on performance.

Keywords: polymer-bonded explosive (PBX), propellant, damage, failure, triaxial compression, bonded particle method

1. Introduction

Many energetic materials, such as propellants and plastic bonded explosives (PBX), belong to the broader class of materials known as highly filled polymer composites. Such composite materials are generally tailored to perform a specific function while also meeting other design requirements, which often results in complex, heterogeneous material structure. For example, in electronics packaging applications, filled polymer composites are used to minimize coefficient of thermal expansion mismatch with printed circuit boards as well as to confer electrical or thermal conductivity [1]. For propellants and PBX, the content of the energetic filler grains is of primary concern for applications, and the polymer binder is crucial to provide a structural matrix that enables net shape manufacturing. In addition, the polymer binder reduces explosive sensitivity to inadvertent mechanical insults during manufacturing and the service lifetime of components. In this work, we focus on polymer bonded energetic materials while noting that the insights presented here are also meaningful for general particulate polymer composites and could possibly extend to granular composites such as concrete or asphalt.

It is well known that violent chemical reactions can be accidentally triggered in energetic materials through mechanical insults at much lower impact speeds than those required for intentional detonation [2, 3]. Additionally, even if the material does not undergo substantial reaction, a mechanical insult may permanently change the material's internal structure such that subsequent insults may induce violent reactions in unknown or unexpected conditions. For example, it has been observed in PBX materials that ratcheted uniaxial stress loading reduces the stiffness of the materials on reloading [4, 5]. These observations are direct evidence that damage accumulates in PBX and propellant materials even at loads well below their ultimate mechanical failure point or reaction threshold. Thus, for robust safety assessments of energetic materials, we must be able to predict the material's mechanical response to a general three-dimensional loading insult and specifically what mechanisms have caused permanent changes to the

*Corresponding Author

Email addresses: jtclemm@sandia.gov (Joel T. Clemmer), knlong@sandia.gov (Kevin N. Long), judbrow@sandia.gov (Judith A. Brown)

composite mesostructure.

The mechanical behavior of PBX and propellant materials is complex. There are known strain rate and temperature dependencies, viscoelasticity due to the polymer binder, damage evolution causing loss of stiffness, tension-compression asymmetry, and pressure-dependent inelastic behavior. An excellent review of the quasistatic mechanical behavior of HMX (1,3,5,7-tetranitro-1,3,5,7-tetrazocane) and TATB (triaminotrinitrobenzene or 2,4,6-triamino-1,3,5-trinitrobenzene) based PBX materials with relevant experimental references is given by Plassat et al. [4]. Other PBX materials [6] and propellants [7, 8] also demonstrate similar features in their mechanical responses. The authors deem pressure-dependent inelasticity to be of particular interest because energetics are frequently used in partially or highly confined environments, and because energetics may be loaded under inertial confinement conditions (uniaxial strain) in accident scenarios due to the intermediate to high strain rates involved.

Despite its applicability, the pressure-dependent response of energetic composites has not been as widely studied in the literature as other mechanical behaviors. The authors know of the following papers containing data that explores pressure-dependent mechanical behavior through triaxial compression testing [5, 9, 10, 11, 12, 13, 14, 4, 15]. Weigand and Reddingius [5] studied a surrogate of PBX 9501 under triaxial stress conditions in which the surrogate material was subjected to varying confining pressure at room temperature and then axially strained to failure in compression. They observed two distinct regimes of mechanical behavior in the axial stress versus axial strain signal, a brittle regime with strain softening and localized deformation at low confining pressures and a ductile regime with strain hardening and no clear failure at high confining pressures. As the confining pressure increased, the material response continuously transitioned from the brittle to ductile behavior. Later, Weigand, Leppard, et al. [13] studied additional HMX-based PBX materials under the same triaxial loading setup and largely arrived at the same observations and conclusions.

Rangaswamy et al. tested PBX 9501 under a triaxial compression setup in which both the axial and radial strains were captured under different confining pressures [11]. These studies found that the net volume strain was positive (increase in volume) despite the fact that the material was under a confining pressure and axial compressive load. The HMX-based PBX material M1 has been extensively characterized by the CEA (Commissariat à l'Énergie Atomique et aux Énergies Alternatives) and the Gabriel LaMé Laboratory, including various triaxial compression tests with cyclic loading/unloading [10, 9, 12, 14]. These tests include measurements of both axial and radial strains and also showed a transition from strain softening to strain hardening, pressure-dependent Young's modulus, positive volume strains (i.e. compaction dilation), and the accumulation of plastic (permanent) strains between cycles. The recent review paper by Plassat et al. [4] includes new data on the TATB-based material M2 and demonstrates its behavior under axial confining pressures up to 10 MPa. Lastly, Chatti et al. have tested a PBX-simulant material in triaxial compression up to 10 MPa as well as other multiaxial tests to investigate failure mechanisms [15]. At this time, the authors do not know of any triaxial compression studies on propellant materials, but we expect their behavior to be generally similar since they also fall into the class of highly filled polymer composites and exhibit similar mechanical properties in other uniaxial tests [7, 8].

It is also noteworthy that most of the above studies on pressure dependence were for PBX materials where the binder glass transition is well below room temperature, so that the binder was in its rubbery state during room temperature loading. The only known exception to this is the studies on the TATB-based material M2, which has a glass transition temperature T_g of approximately 60°C [4] and thus was well into its glassy state during the reported triaxial tests. Since the stiffness of the binder material has been shown to significantly influence mechanical deformation mechanisms [16], it is of keen interest to better understand the regime of behavior where the binder material is loaded in the glassy state. We note that this regime is also relevant to materials with T_g less than room temperature as components may see both cold and hot extreme temperatures during their service life.

The observed macroscale effects of damage accumulation (loss of stiffness), permanent plastic strains, volumetric dilation, and their dependence on confining pressure are tied to inelastic mechanisms occurring at the mesoscopic length scale of interactions between the composite PBX material constituents. A key mechanism of microcrack formation that has been observed under uniaxial compression and Brazil tests is delamination between the binder phase and granular filler phase [17, 18, 19, 20]. It can also be inferred that the permanent positive volume strain observed during triaxial compression must be related to opening of void space (porosity) in the PBX material microstructure. This opening of volume strain or shear-induced dilation [21] is a signature of granular materials and soils, which will be important in modeling considerations for both quasistatic [4, 22, 23, 24] and higher strain rate loadings [25, 10, 14]. Material properties that govern the interplay between these mechanisms include interfacial strength between the energetic filler and binder phases and the properties of the binder itself, including its glass transition temperature and any nonlinearities in its viscoelastic behavior [16]. A good example of such a binder is HTPB (hydroxyl-terminated polybutadiene), which exhibits strong nonlinearity and some plastic deformation behavior due to its hard and soft polymer segments [26, 8, 7].

For general three-dimensional loading of polymer bonded energetic materials, any or all of the above mechanisms may be active [25, 23, 4]. Thus, a predictive macroscale constitutive model must be able to accurately represent each of the observed inelastic mechanisms (viscoelasticity,

damage, and accumulation of permanent strain) as well as their complex interplay. Current constitutive models in the literature have tried to represent each of these three main mechanisms with varying degrees of complexity and predictive fidelity [4]. However, the pressure-dependent inelastic responses of these models are the least well defined and characterized of the different inelastic mechanisms for existing constitutive models today. To the authors' knowledge, constitutive models in the literature have assumed that the pressure-dependent inelastic behavior can be represented by a viscoplastic Drucker-Prager type yield surface [22, 23, 10, 25], a Mohr-Coulomb yield surface [27, 28, 29], the Karagozian & Case model [30], or a Bodner-Partom viscoplastic model [31, 32]. Other constitutive models do not include plasticity [7, 8, 33, 34, 35]. However, with the limited data available, the validity of these model choices for arbitrary materials and stress states is unknown, especially when one considers the broad range of binders and their corresponding glass transitions available in different energetic composites as well as the range of energetic filler volume fractions. The review work in [4] recognized the need for micromechanics simulations to elucidate the correlations between mesoscale mechanisms and macroscale behaviors. There have been many excellent mesoscale models of PBX, but most of these have focused on hot spot formation under impact loads (e.g. Refs.[36, 37, 38, 39]) or detailed studies of crystal and interface properties containing a small number (< 100) of grains (e.g. Refs. [40, 26]) rather than computational homogenization of behavior across large, representative volume elements.

To address these knowledge gaps, we present a bonded particle model (BPM) that enables us to directly correlate the activation of inelastic mechanisms on mesoscopic scales with macroscale constitutive behaviors across a broad range of composite material design parameters. The advantage here lies in the computational efficiency of the BPM and avoidance of the mesh-generation bottleneck that is faced through more traditional finite-element-based mesoscale approaches. As in other particle-based methods, discontinuities due to cracks or free surfaces are naturally handled in a BPM. Using BPMs, we are able to explicitly model the individual polymer binder and granular filler constituents in fully three-dimensional mesoscale simulations containing 1,024 filler grains. The scale of such simulations enables novel studies that can rigorously link microscale deformation mechanisms with emergent macroscale mechanical behavior.

In this work, we systematically study the effects of polymer binder behavior and interfacial filler-binder adhesive strength on the triaxial response of idealized highly filled polymer composites representative of propellant and PBX materials. Limiting case properties are used to explore the wide material design parameter space rather than focusing on a single, specific material formulation. This allows us to provide a broad, unified perspective that holds across the diverse range of polymer bonded energetic materials and potentially extend to other classes of highly filled, bonded granular composites. In Section 2 we describe the BPM used to conduct mesoscale simulations, define the limiting cases of various binder and filler-binder interface properties, and discuss the deformation protocol. Results are presented in Section 3, with discussion of predicted global stress-strain behavior in Subsection 3.1, discussions of inelastic mechanisms in Subsections 3.2 and 3.3, and an exploratory study on the effects of Lode angle comparing triaxial compression with triaxial extension stress states in Subsection 3.4. Several conclusions that will be useful to guide macroscale constitutive model development, experimental characterization strategies, and future material design from a mechanical behavior perspective are given in Section 4.

2. Method

2.1. Model Description

To simulate the loading and failure of polymer bonded granular composites, we use a bonded particle model (BPM) which, at its core, is a breakable spring network. This model was implemented in LAMMPS [41] using a publicly available BPM package developed at Sandia National Laboratories. Solids are represented by a set of point particles, akin to the BPM studied in Ref. [42], each with mass m and diameter d. Note that our use of the word particle only refers to the fundamental simulation unit in this paper and not the granular filler phase of a composite. To create a foundation for a composite solid, a cubic box with a side length of $200d$ and periodic boundary conditions is randomly filled with nearly 10 million particles such that their cumulative volume is 64% of the total system volume. Large overlaps are then removed by applying a soft repulsive force between particles and running overdamped dynamics. This protocol yields an isotropic packing near the zero pressure jamming limit. All numerical integration uses the velocity-Verlet algorithm.

Within this system, all pairs of particles within a distance of $1.5d$ are then connected with bonds resulting in approximately 15 bonded neighbors per particle. The equilibrium length r_{eq} of each bond is set to the initial distance between the two particles r_0 creating a stress-free reference state. Note that this system does not yet have any mesostructure: there is no distinct filler or binder phase.

If a bond is stretched or compressed from its initial state, one component of the force between the two particles separated by a displacement $\vec{r}$ is given by

$$\vec{f}_B(\vec{r}, r_{\text{eq}}) = \hat{r} \begin{cases} 0.5 k_b r_{\text{eq}} \left([r_{\text{eq}}/r]^2 - 1 \right) & \epsilon \leq 0 \\ -k_b r_{\text{eq}} \epsilon & 0 < \epsilon \leq \epsilon_p \\ -k_b r_{\text{eq}} \epsilon_p & \epsilon_p < \epsilon \leq \epsilon_{\max} \\ 0 & \epsilon > \epsilon_{\max} \end{cases} \tag{1}$$

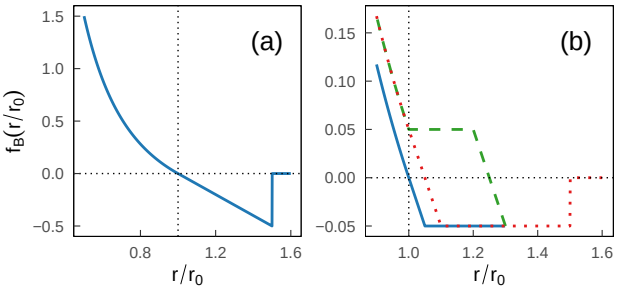

Figure 1: Magnitude of the bond force as a function of r/r_0 for $k_b = 1$, $\epsilon_{\max} = 0.5$, and ϵ_p equal to (a) 0.5 or (b) 0.05. In panel (b), the force depends on the loading history as r_{eq} evolves. The bond starts at $r/r_0 = 0.9$ and is loaded in tension up to $r/r_0 = 1.3$ (solid, blue). The bond is then unloaded back to $r/r_0 = 0.9$ in compression (dashed, green) before reloading in tension up to $r/r_0 = 1.6$ causing it to break (dotted, red).

where r is the magnitude and $\hat{r}$ is the unit vector of $\vec{r}$, k_b is a stiffness, $\epsilon \equiv r/r_{\text{eq}} - 1$ is a strain, ϵ_p is a plastic onset strain, and $\epsilon_{\max}$ is the limiting strain for a bond to break. In compression, $\vec{f}_B(\vec{r}, r_{\text{eq}})$ is repulsive and is approximately linear with a stiffness k_b at small displacements but diverges as $r \to 0$ to ensure particles can never fully overlap. In extension, the force is attractive and is also linear up to a strain of ϵ_p (if $\epsilon_p < \epsilon_{\max}$) at which point it plateaus until the bond breaks at $\epsilon = \epsilon_{\max}$.

To model elastic bonds, we set $\epsilon_p = \epsilon_{\max}$ such that bonds have no plastic component as illustrated in Fig. 1(a). In these elastic bonds, the equilibrium length r_{eq} never evolves. To add plasticity, we set $\epsilon_p < \epsilon_{\max}$ such that the bond has a perfectly plastic regime. Plasticity is first activated when ϵ reaches ϵ_p in tension after which r_{eq} will track the current value of the strain in both extension and compression, lagging it by $\pm\epsilon_p$ depending on the loading direction. However, r_{eq} is not allowed to drop below r_0 even if the bond compresses to $r < r_0$. In this limit, the diverging repulsive force in Eq. (1) will be vertically shifted by the last value of the force to maintain continuity as illustrated in Fig. 1(b). Similar bond models have also been proposed to simulate plasticity [43] based on a more common type of BPM where particles have rotational degrees of freedom as in the discrete element method [44].

To remove excess kinetic energy produced during deformation, bonds also exert a drag force. This drag force does not depend on the history of the bond and is given by

$$\vec{f}_{B,D}(\vec{r}, \Delta\vec{v}) = -\Gamma(\hat{r} \cdot \delta\vec{v})\hat{r} \tag{2}$$

where Γ is a damping strength and $\delta\vec{v}$ is the relative velocity of the particles. Only the radial component of $\delta\vec{v}$ is damped to conserve linear and angular momentum of solid bodies [45]. Without this damping term, the kinetic energy of the system would continue to rise during shear and could thermalize particles.

When a bond irreversibly breaks in tension, it can be thought of as the nucleation or growth of a crack. If two unbonded particles, either on opposite sides of a crack or from separate solid bodies, come into contact such that $r \leq d$, they experience an additional purely repulsive force:

$$\vec{f}_P(\vec{r}, \delta\vec{v}) = \frac{k_p r_c}{2}\left(\frac{r_c^2}{r^2} - 1\right)\hat{r} - 10\Gamma\delta\vec{v}\left(1 - \frac{r^8}{r_c^8}\right) \tag{3}$$

where k_p is a stiffness and $r_c = 0.95d$ is the cutoff of the interaction. We choose a contact cutoff slightly smaller than the defined particle diameter to ensure there are no contacts in the initial system if bonds were removed. As before, the repulsion approximates a linear spring of stiffness k_p at small overlaps but diverges with increasing overlap to prevent particles from ever collapsing under large stresses. However, the damping now applies tangential forces and the multiplicative factor on the damping smooths the strength of the damping force to zero as particles come out of contact. We refer to this as a pair interaction as opposed to a bond interaction based on the standard LAMMPS nomenclature. Pair interactions are not applied between bonded particles.

2.2. Mesostructure and Model Parameters

To create the mesostructure of composites, we first generate five different packings of 1,024 frictionless, monodisperse spheres at 64% volume fraction using a protocol similar to that described in Sec. 2.1. These smaller packings serve a geometric template or stencil representing the granular filler phase in a representative volume (RV) of the composite system. The stencil is scaled and overlaid on the original large packing to identify whether each particle belongs to the granular filler or binder phase (whether or not a particle resides within one of the scaled up spheres). Bonds that connect two particles in different spheres are broken to remove any cohesive forces between separate bodies in the granular filler. An example of a resulting two-phase system is rendered in Fig. 2. Statistical analysis of these representative volume (RV) mesostructures is provided in Appendix A to establish isotropy and to show that the RVs are sufficiently large such that fluctuations in homogenized behaviors among them are minimal compared to the mean of those quantities of interest. While the volume fraction of granular filler is relatively low compared to typical PBXs or propellants, a random close packing of monodisperse spheres serves as a simple and easily reproducible starting point. In future work, this procedure could be adjusted to use aspherical or polydisperse granular bodies with different binder fill fraction to more accurately represent specific material formulations.

Based on the identity of two interacting particles, different interaction parameters are used to model different material responses. There are three bond stiffnesses, $k_{b,BB}$, $k_{b,BG}$, and $k_{b,GG}$, and three pair stiffnesses, $k_{p,BB}$, $k_{p,BG}$, and $k_{p,GG}$ corresponding to binder-binder, binder-grain, and grain-grain interactions, respectively. Recall that bond stiffnesses correspond to cohesive material responses while pair stiffnesses correspond to contact interactions between distinct solid bodies. We base the units

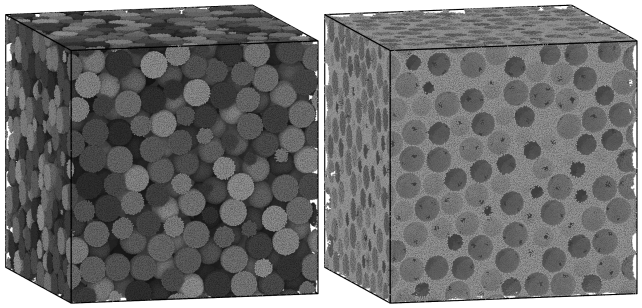

Figure 2: Renderings of the (left) granular filler and (right) binder phases of a system at initialization. Each phase is represented by many particles with over 5,000 particles per filler grain.

of the simulation on the solid binder phase and therefore define $k \equiv k_{b,BB}$. Using this definition, we then set $k_{b,BB} = k_{b,BG} = k$ and $k_{b,GG} = 10k$ such that the granular filler phase is ten times stiffer than the binder phase and grains can be approximated as rigid bodies that translate and rotate. We note that this assumption minimizes deformation and prevents cracking within filler grains in our model. While this mechanism has been observed in some energetic materials, it is the least common mechanism seen in quasi-static experiments [20, 19, 17, 46, 16], which is the regime of interest in this article.

For pair forces, we set $k_{p,BB} = k_{p,GG} = k_{p,BG} = k$, noting that grain-grain bonds do not break such that pair forces are never exposed. The fundamental units of our simulations are then k, m, and d from which a unit of time can be defined $\tau = \sqrt{k/m}$. We use a time step of $\Delta t = 0.05\tau$ and a constant damping strength of $\Gamma = m/(10\tau)$ for all interactions.

Similarly to the stiffness, there are distinct values of the strains at which a bond breaks, $\epsilon_{\max}$, and plastically activates, ϵ_p, for the three types of bonds. In the granular filler phase, we set $\epsilon_{\max,GG}$ sufficiently high that bonds never break and set $\epsilon_{p,GG} = \epsilon_{\max,GG}$ so bonds are always elastic although future work could consider inelasticity in the grains. We also choose to fix $\epsilon_{\max,BB} = 0.5$ and $\epsilon_{p,BG} = \epsilon_{p,BB}$ leaving two free parameters, $\epsilon_{p,BB}$ and $\epsilon_{\max,BG}$. Tuning $\epsilon_{p,BB}$ controls the onset of plasticity in the binder phase while tuning $\epsilon_{\max,BG}$ sets the interfacial strength between the binder and the grains.

To represent the material design cases with varying binder T_g and filler-binder interfacial strength, we consider four sets of parameters listed in Table 1. First are the two elastic binder cases which are representative of a binder with a low glass temperature T_g relative to the operating temperature of the composite. Here the binder is fully elastic (representing elastomer-like behavior), but the interface is either just as strong as the bulk (elastic/strong), or the interface is much weaker than the bulk and fails at strains of 5% (elastic/weak). Next there are two elastic-plastic binder cases which idealize composite behavior op-

	Elastic binder	Plastic binder
Strong interface	$\epsilon_{p,BB} = 0.5$ $\epsilon_{\max,BG} = 0.5$	$\epsilon_{p,BB} = 0.05$ $\epsilon_{\max,BG} = 0.5$
Weak interface	$\epsilon_{p,BB} = 0.5$ $\epsilon_{\max,BG} = 0.05$	$\epsilon_{p,BB} = 0.05$ $\epsilon_{\max,BG} = 0.05$

Table 1: Values of cohesive failure strain, $\epsilon_{\max}$, for binder-grain bonds and plastic onset strain, ϵ_p, for binder-binder bonds used in the four material models.

erated well below T_g of the binder. The simplest description of glassy polymer behavior is that of elastoplasticity [47]. The elastic-plastic binder bonds idealize this behavior. Here the binder experiences plasticity at 5% strain and the interface is either strong (elastic-plastic/strong) or weak (elastic-plastic/weak).

To calibrate the small-strain, linear-elastic material properties of the system, we generate a bulk sample of binder which is isotropically compressed and expanded to calculate a bulk modulus of $B \approx 1.24k/d$. Analogously, this implies the granular phase will have a bulk modulus of $12.4k/d$. In the remainder of the text, all reported pressures and stresses are normalized by the bulk modulus of the binder phase. Since our model is built on central, pairwise forces acting between an isotropic set of particles, both phases have a Poisson's ratio of 1/4 [48]. While this Poisson ratio is low for both the polymer binder glass and elastomer limits, the focus of this work is on the role of inelastic mechanisms of plasticity and interfacial failure, and so this error in binder cohesive compressibility is tolerated to enable pursuit of a relatively simple but flexible model. In the future, we hope to use a non-local bond model to allow independent control of Poisson's ratio, which will allow us to explore the importance of binder compressibility relative to the other deformation mechanisms.

2.3. Deformation Protocol

For theoretical simplicity, we consider loading paths at a constant mean pressure $P = -\mathrm{Tr}(\sigma)/3$ where σ is the stress tensor. Therefore, all loading paths reside in the π plane in stress space with a normal vector along the line of constant mean pressure and an intersection at P. The stress tensor is calculated as the sum of the kinetic and virial components using the volume of the simulation box as a normalization. This measure of the stress has been found to reproduce the continuum Cauchy stress [49]. As we are interested in pre-fracture behavior, we do not worry about the disconnect that emerges between the volume of the simulation cell and the material volume when the system breaks apart and creates void space. However, as identified in Subsection 3.1, the elastic/weak case can dilate post-yield due to pores opening up at granular-binder interfaces which does affect our stress metric.

To maintain a constant mean pressure during deformation, we use a linear pressure control that isotropically scales the lengths of each dimension of the simulation box

by a dilation factor D proportional to the deviation from the target pressure P_T. This factor is calculated at every increment of time t as

$$D(t) = (1 + c_g[P(t) - P_T]\Delta t)^{1/3} \tag{4}$$

where $c_g = 10^{-3}d/(k\tau)$ is a gain coefficient which is capable of maintaining the target pressure within a factor of ~ 0.003 in all simulations up until the system fractures. Note that the true stress tensor is used for the prescription of pressure control as well as for the extraction of other stress components described later in the text.

To generate shear in triaxial compression (TXC), the z dimension is additionally compressed at a strain rate $\dot{\epsilon}_z = -2\dot{\epsilon}/\sqrt{3}$ while the x and y dimensions are extended at rates of $\dot{\epsilon}_x = \dot{\epsilon}_y = -\dot{\epsilon}_z/2$ where $\dot{\epsilon}$ is the square root of the second invariant of the deviatoric strain rate tensor: $\sqrt{\dot{\epsilon}_x^2 + \dot{\epsilon}_y^2 + \dot{\epsilon}_z^2}/\sqrt{2}$. The shear strain of the system is then defined as the product $\dot{\epsilon}t$. The true (logarithmic) strain tensor is used for the prescription and extraction of strain tensor components. In Sec. 3.4, we consider the opposite case of triaxial extension (TXE) where the strain rate on each dimension is simply inverted.

Combining the pressure control with the shear strain, the size of the simulation box L along a direction α evolves according to:

$$L_\alpha(t + \Delta t) = L_\alpha(D(t) + \Delta t\dot{\epsilon}_\alpha) \tag{5}$$

where we set $\dot{\epsilon} = 10^{-6}/\tau$ to minimize finite rate effects and represent quasistatic strain. As the box deforms, particle positions are affinely shifted every timestep to track the deformation. To accomplish this, the particles' x, y, and z coordinates are simply scaled to match the expansion or contraction of each box dimension so a particle's relative position in the box is unchanged by the deformation protocol. This allows us to deform the periodic system without defining boundaries. Forces between particles then induce nonaffine particle motion. A similar protocol was used in Ref. [50] to study the steady-state rheology of dry granular materials. For each of the five RVs, simulations were run under both TXC and TXE for all four of the material models in Table 1 at constant mean pressures of 0, 4, 8, 16, 24, and 32% of the binder bulk modulus.

3. Results and Discussion

3.1. Macroscopic Stress Response

In this section, we focus on the global stress response of systems in TXC to identify how and when the four material models deviate from elastic loading under increased confining mean pressure. In the following two sections, we will then delve into the microscopic and mesoscopic behavior of the system and compare it to the macroscopic behavior. For this discussion, we define macroscale as the full system (the whole RV), mesoscale as the size of filler granules, and microscale as subgranular length scales based on the underlying particles of our simulation. Finally, in Sec. 3.4 we will briefly discuss the mechanical responses to TXE loading in contrast to TXC.

As the pressure P is held constant, we focus on the deviatoric stress tensor with components $s_{ij} = \sigma_{ij} - P\delta_{ij}$ where σ is the full stress tensor and δ_{ij} is the Kronecker delta. Two important metrics that define the stress state of the system are then the second,

$$J_2 = \frac{1}{2}\left(s_1^2 + s_2^2 + s_3^2\right) \quad , \tag{6}$$

and the third,

$$J_3 = \frac{1}{3}\left(s_1^3 + s_2^3 + s_3^3\right) \quad , \tag{7}$$

invariants of s where s_1, s_2, and s_3 are its principal components. We quantify the magnitude of the deviatoric stress as the square root of J_2, which we refer to simply as the shear stress, and measure the directionality of shear in terms of a Lode angle θ:

$$\theta = \frac{1}{3}\arcsin\left(\frac{J_3}{2}\left[\frac{3}{J_2}\right]^{3/2}\right) \quad . \tag{8}$$

In this definition, a TXC stress state corresponds to $\theta = -\pi/6$ while TXE corresponds to $+\pi/6$.

In an analogous fashion, one can define a Lode angle for the strain tensor of the system which is kept fixed in a strain-imposed deformation protocol. While the stress and strain tensors may not have equivalent Lode angles under general loadings, as seen in dry granular loading [51], we find agreement in the two extremes of TXC and TXE where deformation is cylindrically symmetric noting that the studied mesostructures are statistically isotropic. During loading, θ rapidly approaches the expected value of $-\pi/6$ in TXC (or $\pi/6$ in TXE) and fluctuations do not exceed a few percent until the system fails.

More informative is the magnitude of the shear stress. In Fig. 3, the shear stress is plotted as a function of strain for each material model listed in Table 1 at different mean pressures P. Stress-strain curves are based on a single representative mesostructure realization, however, minimal deviations in the mechanical response were found across the five mesostructure realizations as discussed in Appendix A. At small strains, all curves exhibit the same linear increase in stress. We denote the end of the linear regime as yield, which can depend heavily on confining mean pressure and is marked by a symbol on Fig. 3. Specifically, we define yield by fitting a linear regression to the first 1% strain and identifying when the extrapolation deviates from the data by 10%. Yield is also restricted to be less than or equal to the peak stress. This definition of yield is similar to those used in other studies of polymer bonded energetic materials (see, for example, [13]). Between yield and failure, the latter defined as the peak stress and designated using an outlined symbol, one can identify a wide range of phenomenologies including brittle

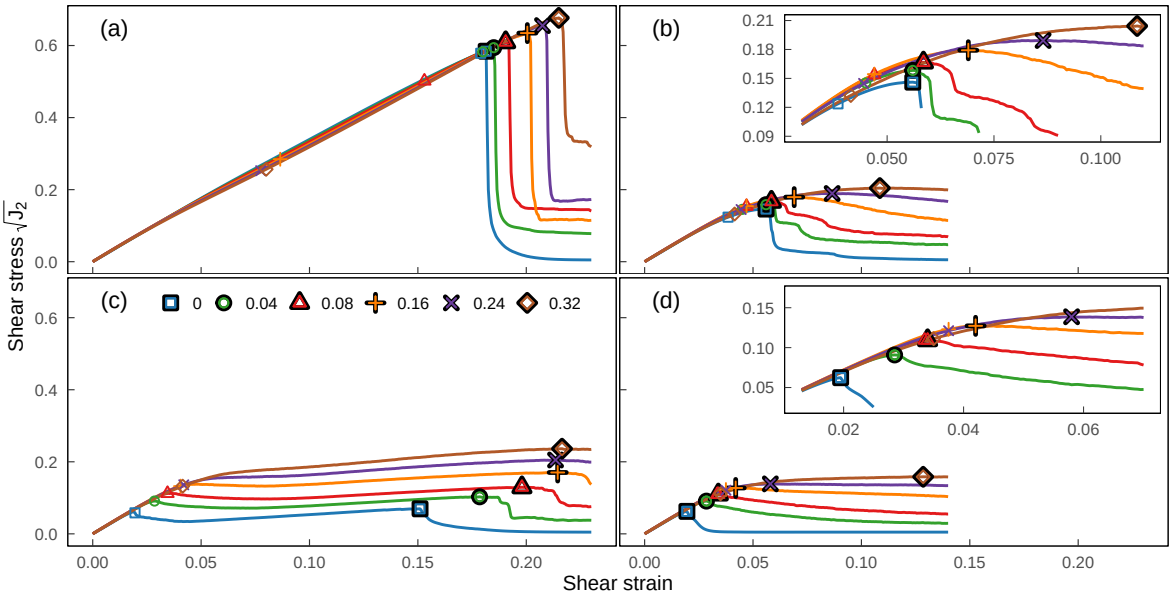

Figure 3: Example curves of the shear stress as a function of strain in TXC under pressures P indicated in the legend using the (a) elastic/strong, (b) elastic-plastic/strong, (c) elastic/weak, and (d) elastic-plastic/weak material models listed in Table 1. The location of yield (no outline) and peak stress (black outline) are indicated by symbols on each curve.

failure, strain hardening, and strain softening depending on the binder behavior and interfacial strength. As with all other values of stress and pressure included in the text, shear stresses in Fig. 3 are normalized by the bulk modulus of the binder. Unless otherwise noted, all figures in this article are based on the same mesostructure realization and use the same symbols to designate yield and failure strains.

Simulations of elastic/strong systems (Fig. 3[a]) display typical brittle behavior under small pressures where both yield and failure nearly coincide and are followed by a rapid drop in stress. Failure occurs by the rapid growth of a percolating crack that spans the length of the RV in the dimension of axial compression. With higher mean pressures, the system strengthens and is able to support higher peak stresses. In addition, there is a slight splay in stress-strain curves at intermediate strains with increasing P introducing a pressure dependence to yield which is highly sensitive to the 10% deviation threshold used in the definition. While we do not know the exact origin of this effect, it may be due to binder bonds breaking earlier in the interstitial region between two relatively stiff filler granules which may induce excess nonaffine particle rearrangement and deviation from linear behavior.

In the more interesting elastic-plastic/strong case where the binder allows plastic deformation (Fig. 3[b]), yield occurs much earlier at strains slightly less than 5% (the bond criteria to induce plasticity). Above yield, the stress-strain curve slope is gradually reduced until peak stress and failure occurs. With increasing P, this regime extends to larger strains before a less abrupt decrease in stress at failure. At low P, the system dilates with shear (positive volume strain) while at higher P the system initially contracts before dilating as seen in Fig. 4(b).

If the binder is poorly adhered to filler granules, there is an expected reduction of the maximum strength of the composite under all conditions. In the elastic/weak system (Fig. 3[c]), yield occurs at a significantly smaller strain associated with the breakage of binder-grain bonds and subsequent separation of granules from the binder. At small P, the post-yield behavior shows a strain-softening regime followed by a gradual strain-hardening regime. As P increases, there is less post-yield strain softening, and failure is delayed until a larger strain. This continues until reaching a mean pressure of $P \sim 0.24$ at which the strain-softening regime disappears and the strain of failure no longer has a significant dependence on increasing P. The intermediate loading regime between yield and failure is associated with dilation even at high P as seen in Fig. 4(c).

With an elastic-plastic/weak binder (Fig. 3[d]), a transition with increasing P is also seen. At low confining pressure, failure coincides with or quickly follows yield while a hardening regime emerges at high confining P. Similar to the elastic-plastic/strong case, dilation before failure is only seen at low confinements (Fig. 4).

Yield and peak stresses in all systems are aggregated in Fig. 5 and plotted as a function of P. Stress values are averaged across all RV mesostructures and error bars indicate the standard deviation of each metric across RVs emphasizing minimal variations and suggesting there are sufficiently many granules. Both metrics generally increase with P with the exception of yield in the elastic/strong case where yield is heavily dependent on the definition as

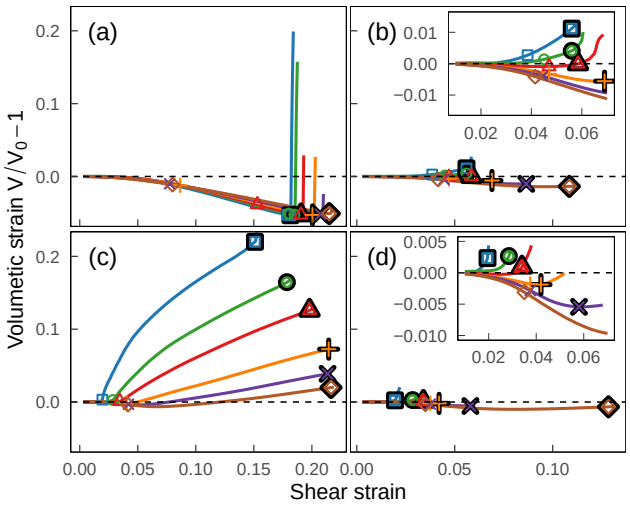

Figure 4: Volumetric strain, calculated using the ratio in the current volume V to initial volume V_0 of the system, as a function of shear strain at different P. Note that the horizontal axes are not consistent across columns. Systems correspond to the (a) elastic/strong, (b) elastic-plastic/strong, (c) elastic/weak, and (d) elastic-plastic/weak binder models listed in Table 1. The location of yield (no outline) and peak stress (black outline) are indicated on each curve by symbols. Insets highlight data near yield in elastic-plastic cases.

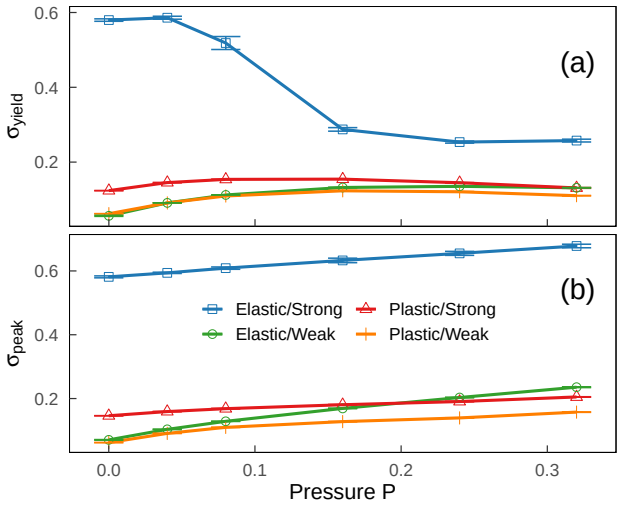

Figure 5: Average (a) yield and (b) peak stress as a function of mean pressure P for the binder models indicated in the legend. Error bars represent standard deviations across mesostructure realizations.

discussed above.

Independent of any particular material calibration, the simulated behaviors in Figs. 3 and 4 still demonstrate a good qualitative resemblance to high and low T_g (relative to room temperature) plastic bonded explosives data in the literature. Here, we reproduce triaxial compression data for a high glass transition composite, M2 from Ref. [4], in Fig. 6(a-b), and for a very low glass transition composite, EDC37 from Ref. [13], in Fig. 6(c). Before drawing qualitative comparisons, however, we must note a few caveats to aid interpretation. In both sets of experiments from the literature, the boundary conditions were slightly different from our methods here. Experimentally, the radial (also called the lateral) pressure was held constant while the axial stress was independently varied. Consequently, the mean pressure varied throughout the test as one can see in the M2 material in Fig. 6(a). In contrast, all simulations in this article occurred under a constant mean pressure P up to failure. Moreover, we do not know the strength of the interface between the binder and particle phases in the literature materials but assume that these would be bounded by the "strong" and "weak" cases explored here. We also presume that the high T_g binder in M2 would be most similar to an elastic-plastic response while the low T_g EDC37 binder would be most-similar to our simplified linear-elastic binder systems. However, there is an important implication of our modeling choice of fixing a constant bond stiffness in the elastic regime across all cases that must be considered when comparing to specific materials. The behavior of polymers is known to be viscoelastic and thus the material's stiffness will vary above and below the glass transition, with stiffer behavior below T_g and softer, more rubbery, behavior above T_g. This accounts for the much higher magnitude of pre-yield stresses supported by the M2 material than EDC37 at comparable pressures (Fig. 6). Since the elastic stiffness in all simulations is the same, the magnitude of stresses is only affected by the inelastic deformation mechanisms and is much closer between our elastic-plastic and elastic binder cases.

Even with these assumptions, one can see similar trends between the elastic-plastic/weak case, Fig. 3(d), and the M2 material, Fig. 6(a-b). The corresponding simulations at constant mean pressure show first compressive volume strain followed by dilation post-yield (Fig. 4[d]) which is conceptually similar to the transitions from volume compression to volume dilation seen in the M2 material at its yield point (Fig. 6[a]). Moreover, for both the elastic-plastic/weak modeling and M2 experiments, the yield stress clearly increases with mean pressure. Interestingly, the deviatoric stress versus deviatoric strain from M2 shows little change with increasing confining pressure in contrast to the the transition from softening to hardening behavior post yield as the mean pressure increases for the elastic-plastic/weak simulations (Fig. 3[d]). This latter difference may be due in part to the difference in boundary conditions, and future work must investigate the difference between mechanical responses at constant mean pressure versus constant radial pressure. Additionally, since the grain-binder interfacial strength in M2 is unknown, it is reasonable to hypothesize that the materials response would likely be somewhere between our elastic-plastic/weak and elastic-plastic/strong cases where only strain-hardening behavior is seen.

For the elastic/weak case, Fig. 3(c), the simulation responses are relatively straightforward to compare to the

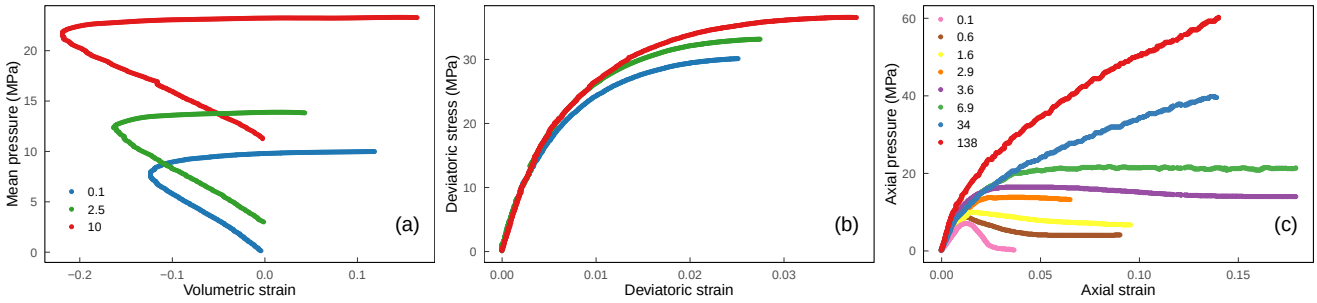

Figure 6: Experimental data from TXC tests of (a-b) M2 [4] and (c) EDC37 [13]. (a) The mean pressure as a function of volumetric strain in M2 samples held at a constant confining radial (or lateral) pressure indicated by the legend in MPa. (b) Deviatoric stress versus strain for the same systems in (a). In (c), axial stress is plotted versus axial strain from EDC37 samples held at a constant radial (or lateral) pressure indicated by the legend in MPa.

low T_g binder PBX material EDC37 in Fig. 6(c). At low confining pressures, both experiments and simulations yield and then soften and fail abruptly. However, as the confining pressure increases, the behavior transitions from strain softening to a strain plateau to substantial strain hardening. The simulations clearly show that the post-yield behavior is associated with substantial dilation (Fig. 4[c]), which also is evident by pictures of post-mortem specimens from the EDC37 TXC experiments in [13] (not shown). Similar behavior is seen in other low T_g PBX materials, such as PBX 9501 [11] and mock PBS 9501 [5] confirming that our simulations are producing behavior that is qualitatively representative of experimental data.

3.2. Microstructural Response

In the previous section, we demonstrated that these four abstract materials with limiting-case polymer binder and grain-binder interface behaviors have remarkably different stress responses which qualitatively compare to real-world materials. The differences in macroscopic response in these four materials at different mean pressures P ultimately stem from differences in the underlying microstructural dynamics on length scales smaller than the filler grains. While tracking dynamics on this subgrain length scale can be challenging experimentally, this information is readily available from simulations. In this section, we therefore identify how key features in stress-strain curves map to the activation of different inelastic mechanisms on the particle scale, namely bonds breaking and plastically deforming. These metrics are used to contextualize results from the previous section.

In Fig. 7, the fraction of both binder-grain and binder-binder bonds that break are plotted as a function of strain for all material models in Table 1. All four systems show broken bonds of both types, with binder-grain interface bonds breaking first at the lowest strains, followed by some smaller fraction of binder-binder bond breakage. This is consistent with experimental observations under quasi-static, unconfined conditions of the various mesoscale deformation mechanisms which include cracking along grain-binder interfaces and ruptures within the binder [20, 19, 17, 46, 16]. In all of these cases, cracks following the energetic grain-binder interfaces were most common. Ruptures within the binder were also observed to a lesser degree. Intra-granular cracking, which is not included in our model, is noted as the least common mechanism seen in Refs. [20, 19, 17, 46, 16].

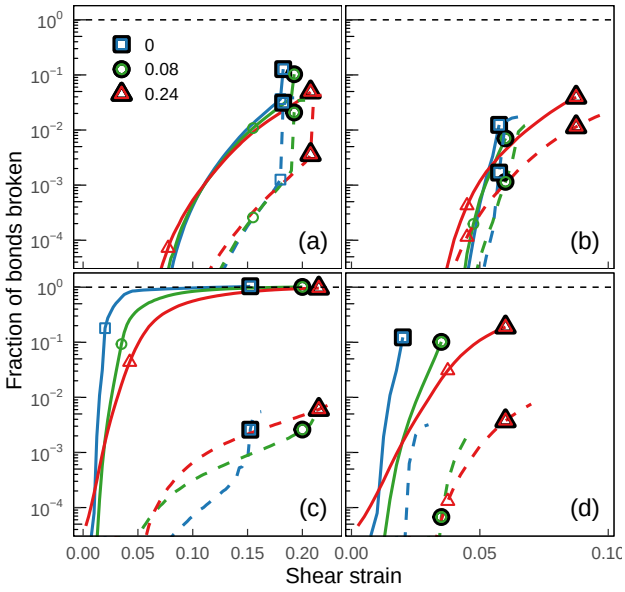

Figure 7: Fraction of interfacial binder-grain (solid lines) and binder-binder (dashed lines) bonds broken as a function of strain at the indicated pressures for the same system in Fig. 3. Symbols indicate approximate locations of yield (no outline) and failure (black outline) within an accuracy of 0.25% strain. The horizontal dashed line represents 100% of bonds. Data is truncated below a fraction of 5×10^{-5} for visibility. Note that binder-grain bonds constitute approximately 14.5% of all bonds in the binder. Systems correspond to the (a) elastic/strong, (b) elastic-plastic/strong, (c) elastic/weak, and (d) elastic-plastic/weak binder models listed in Table 1

In systems with elastic binders, the only inelastic mechanism is the failure of bonds. The simplest case of an elastic/strong system demonstrates typical brittle fracture (Fig. 7[a]). Few bonds break at small strains, consisting mostly of binder-grain or interfacial bonds representing

small microcracks near granular contacts, up until a rapid increase in the number of broken bonds at failure as cracks span the system causing fracture. The most salient trend for this case is that the strain-to-failure is correlated with the mean pressure P in Fig. 5(a). Increasing P slightly broadens the domain of strains where bonds break, which may explain the mild nonlinearities before failure in Fig. 3(a).

In elastic/weak systems, richer behavior is seen in Fig. 7(c). While only a small fraction of binder-binder bonds break preceding failure, significantly more interfacial bonds break at small strains compared to the well adhered system. At low confinement, nearly all interfacial bonds break within a few percent strain after yield as filler granules completely separate from the binder during the strain-softening regime seen in Fig. 3(c). This allows voids to open between granules and the binder, leading to the volumetric expansion seen in Fig. 4(c). With increasing confinement, this effect is muted as grains do not fully separate from the binder until a strain of $\sim 10\%$ at $P = 0.24$. This behavior matches the mechanisms hypothesized by Wiegand et al. [13] to explain the transition from post-yield strain softening to strain hardening observed in EDC37.

More insight is gained through the spatial distribution of broken bonds visualized in Fig. 8. At yield with $P = 0$, the broken interfacial bonds are aligned in system-spanning planes that wrap binder-granular interfaces in Fig. 3(a). While the material can still hold a load and has not failed, such structures can explain the strain softening observed after yield as a network of cracks now spans the material microstructure, and localized deformation will ensue on continued loading at this percolated weakness. It is also noteworthy that this network of cracks is anisotropic from the standpoint of generalized (or non-monotonic) loading beyond yield, which has important ramifications for homogenized constitutive modeling of such materials. In contrast by yield at $P = 0.24$, bonds still break near grain interfaces but these are found in smaller clusters across the system (Fig. 3[c]) explaining the disappearance of a strain-softening regime with increasing P.

Near failure, a similar state is seen at both pressures in Fig. 3(b) and (d) where essentially all grains have broken free from the binder. This observation of widespread bond breakage agrees with the saturation of curves of broken interfacial bonds seen in Fig. 7(c). In the unconfined system, $P = 0$, failure coincides with a visible crack through the binder separating the system. Under confinement, $P = 0.24$, no similarly dramatic behavior is seen which is consistent with the relative rate at which stress decreases in both systems.

In elastic-plastic binder systems, both broken bonds and plastic flow of bonds contribute to the inelasticity. To quantify the extent of plastic deformation, we calculate the fraction of binder bonds that have plastically activated, stretching at least $\epsilon_{\text{pd}} = 5\%$ beyond their initial length in tension as plotted in Fig. 9(a) and (c). Additionally, we also calculated the fraction of plastically activated

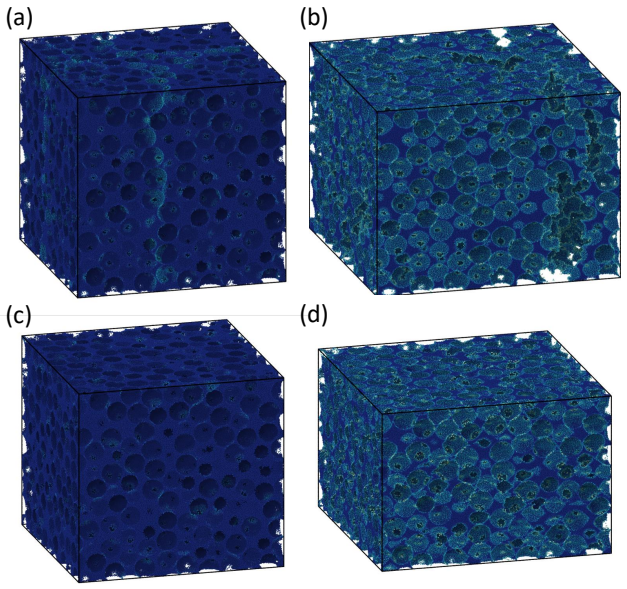

Figure 8: Rendered images of binder particles in the elastic/weak case at a confining pressure of (a-b) $P = 0$ and (c-d) $P = 0.24$. Panels (a) and (c) are just after yield and panels (b) and (d) are just after failure, within a strain of 0.5%. Particles are colored by the number of broken bonds with dark blue corresponding to no broken bonds and tan corresponding to all bonds broken. Images are oriented such that compression is applied vertically while expansion occurs horizontally and into the page.

bonds that broke, seen in Fig. 9(b) and (d), to estimate how many of these bonds utilized the full extent of their plastic elongation. In the elastic-plastic/strong scenario, these metrics include plasticity in both binder-binder and binder-grain bonds. However, in the elastic-plastic/weak scenario, binder-grain bonds break before any plastic deformation (using either definition) such that these metrics only includes binder-binder bonds.

In the elastic-plastic/strong case, both binder-binder and grain-binder interface bonds generally begin breaking before yield and continue to break as the system loads at all P. More interesting trends can be identified in the onset of plasticity in bonds. In Fig. 9(a), fewer bonds have plastically activated with increasing mean pressure. However, in Fig. 9(b), generally more of the plastically activated bonds undergo substantial plastic deformation and break with increasing mean pressure. This suggests that at low P some plastic flow is seen in a much larger fraction of the binder than at high P but significant plastic deformation and failure ends up localizing to a small fraction of these bonds. At high P, a smaller volume of the binder experiences any plastic deformation but the areas that do plastically deform absorb a greater amount of strain and are much more likely to fail than at low P.

During failure, additional insights can be garnered from images of the elastic-plastic/strong system in Fig. 10. At low pressure, bond failure localizes into a few distinct, system-spanning cracks in Fig. 10(a), consistent with the

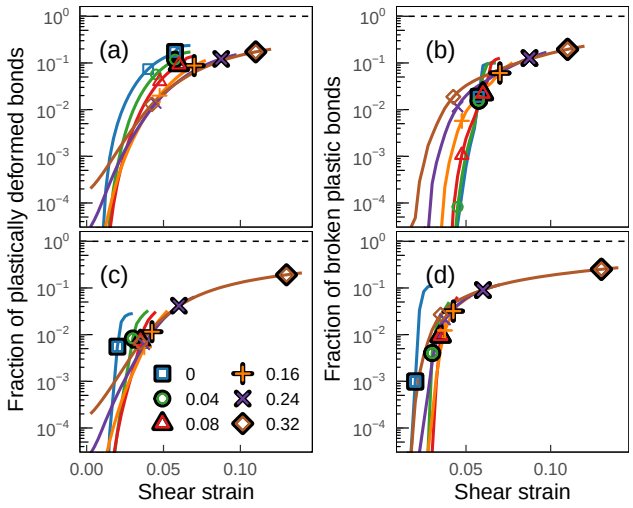

Figure 9: (a,c) Fraction of binder bonds that have plastically deformed by reaching a strain of 5% as a function of shear strain at the indicated pressures. (b,d) The fraction of these plastically activated bonds that broke versus shear strain. Data in the top row corresponds to the (a,b) elastic-plastic/strong case and in the bottom row (c,d) to the elastic-plastic/weak case. Symbols representing yield (no outline) and peak stress (black outline) are placed with an accuracy of 0.25% strain. Data is truncated at fractions of 5×10^{-5}. The horizontal dashed line represents 100%.

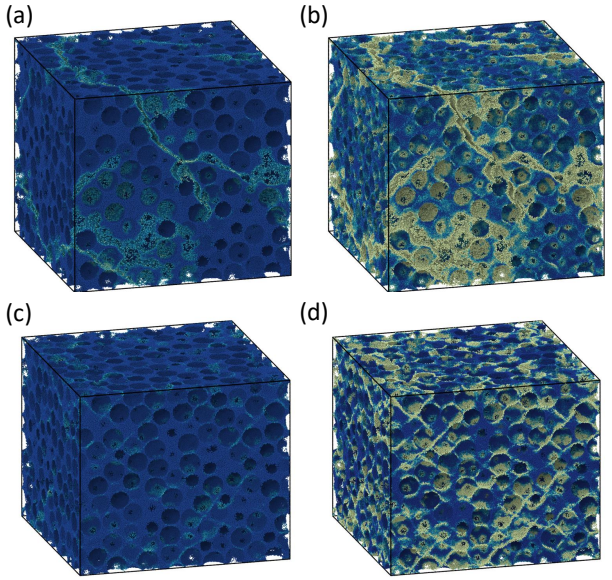

Figure 10: Rendered images of binder particles in the elastic-plastic/strong case at a mean pressure of (a-b) $P = 0$ and (c-d) $P = 0.24$. All panels are just after failure, within a strain of 0.5%. In panels (a) and (c), particles are colored by the number of broken bonds with dark blue corresponding to no broken bonds and tan corresponding to all bonds broken. In panels (b) and (d), color corresponds to the number of bonds that have plastically activated (stretched by at least 5%) with dark blue indicating no bonds have become plastic while tan corresponds to all bonds are plastic.

rapid stress drop at failure. In addition to its presence around cracks, plastic flow is also widely dispersed through out the binder, as seen in Fig. 10(b). In contrast at high pressure, the inelastic mesoscale changes manifest through many smaller cracks that span a few grains as seen in 10(c). Plastic activity is concentrated in these small interstitial regions which allows the system to accommodate strain in these small regions and gradually weaken without dramatic failure. These figures are therefore consistent with our above interpretation

The final case to consider is elastic-plastic/weak systems. At high pressures, $P \gtrsim 0.16$, behavior is qualitatively similar to the elastic-plastic/strong system. With increasing P, the number of plastically activated bonds decreases (Fig. 9[c]) while the fraction of plastically activated bonds that break increases at earlier strains (Fig. 9[d]). It appears that the pressure is able to hold together grain-binder interfaces such that separation of grains from the binder does not fully dominate the dynamics of failure, although the weak interface still reduces the overall strength of the material compared to the elastic-plastic/strong case (Fig. 5[b]).

In contrast, at lower pressures of $P \lesssim 0.16$ different behavior is observed. While the number of plastically activated bonds still slightly decreases with increasing P, the fraction of these that break have an inverted trend to the elastic-plastic/strong case. A greater fraction of plastically activated bonds break at earlier strains with decreasing P. Looking at the fraction of broken bonds, at small pressures the weak interface leads to a rapid rise in the number of broken interfacial bonds at small strains (Fig. 7[d]) in a similar fashion to the elastic/weak case. These cracks at the grain-binder interface place a load on the nearby binder which plastically deforms but ultimately cannot sustain the load causing the system to fracture. This process would explain the brittle-like failure seen in Fig. 5(d) at low pressures and the minimal dilation before failure in Fig. 4(d).

3.3. Mesoscopic Damage: Crack Network Evolution

In continuum modeling of PBX and propellant materials, a damage metric is often used to degrade material stiffness as deformation is incurred (see for example, [35, 7]). The form of this damage metric and its evolution remains an open research question, and it is treated with varying levels of complexity among existing macroscale material models. A detailed discussion of these continuum damage formulations is given in [4], with the conclusion that micromechanical models will have to lead the way and guide our understanding of how the various microcrack systems evolving at the mesoscale interact to drive the overarching macroscale behavior. To this end, we present here an initial analysis of crack network evolution that can be extracted from the BPM simulations.

In addition to monitoring the number of bonds that fail during each simulation, we also record the location and time that they break. This data can then be aggregated to construct the approximate geometries of cracks

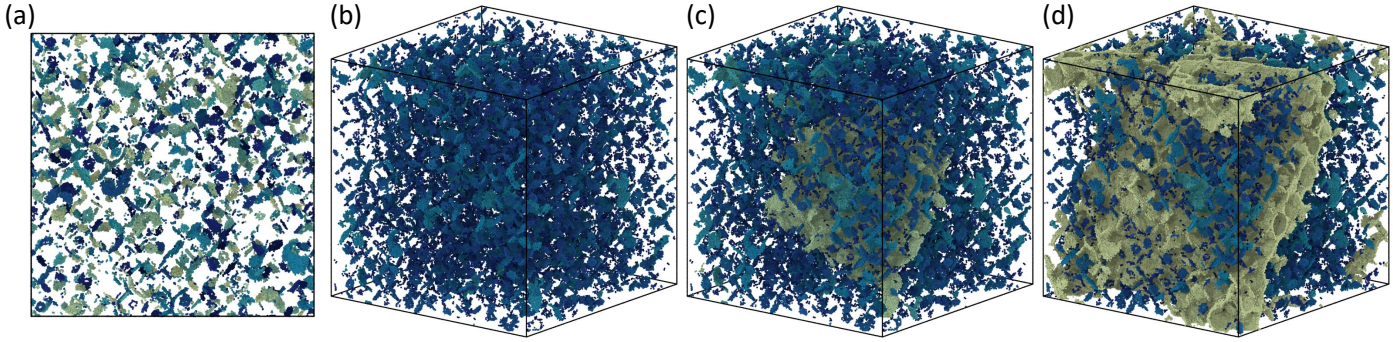

Figure 11: Broken bonds rendered as points in an elastic/strong system at $P = 0$. (a) A cross-section with a width of one quarter of the simulation cell is rendered near failure. Bonds are clustered into distinct cracks each of which is assigned a random color. (b-d) The entire simulation cell is rendered for the same system (b) right before, (c) during, and (d) right after failure where color corresponds to the log of the number of broken bonds in a crack.

in the system at any point in time to provide a mesoscopic perspective on failure that is easier to relate to continuum modeling efforts. This analysis also will provide further insight into spatial correlations of broken bonds, briefly considered in the previous section, to inform the construction of continuum damage models.

To identify distinct cracks, we take the set of all bonds that have broken at a given instant of time and define a spatial location for each bond as the center of mass of the two constituent simulation particles in the undeformed solid. These locations are then discretized onto a cubic grid of cells with side lengths of d, the diameter of a particle. If a cell contains a broken bond, it is flagged. Flagged cells are clustered with their first and second nearest neighbors into connected regions. Each connected region with more than one broken bond is then considered a distinct crack and all constituent bonds are given a shared label. As demonstrated in Fig. 11, which shows the spatial evolution of crack networks in one of the RVs, this allows us to track the nucleation, growth, and coalescence of cracks on a mesoscopic scale as systems load and fail. While this technique is simple, it is prone to overestimate the size of cracks as it fails to account for the orientation of bonds. For instance, if two physically distinct cracks happened to run parallel to each other while separated by a single particle at some location, this method might combine the cracks into a single unit. While it would be useful to develop more sophisticated crack identification techniques in future work, this technique still provides a useful initial interpretation of the large datasets generated during each simulation.

The total number of cracks as a function of shear strain is shown in Fig. 12 for each of the four cases. In the elastic/strong case, this number continues to increase up until failure. In comparison, in the elastic/weak scenario the number of cracks peaks (at smaller strain at smaller P) before decaying up until failure as cracks coalesce. This suggests a relatively small fraction of cracks coalesce in the elastic-strong case until the system actually fails as

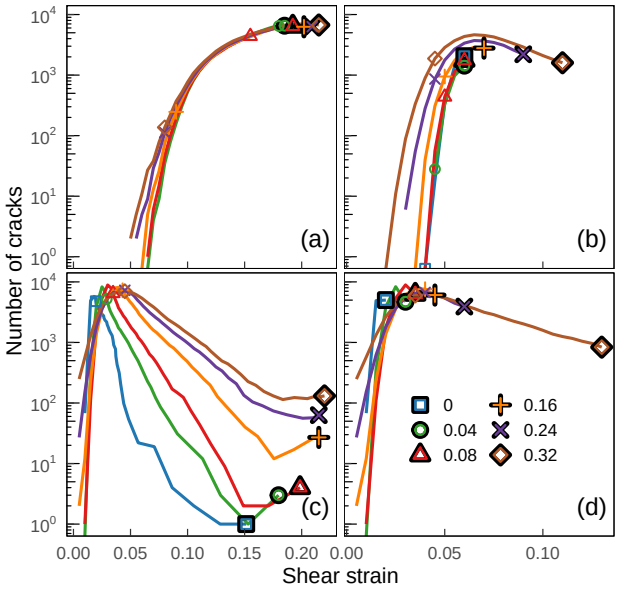

Figure 12: Total number of cracks in the system as a function of strain at the indicated pressures for the same system in Fig. 3. Symbols indicate approximate locations of yield (no outline) and failure (black outline) within an accuracy of 0.5% strain. Systems correspond to the (a) elastic/strong, (b) elastic-plastic/strong, (c) elastic/weak, and (d) elastic-plastic/weak binder models listed in Table 1.

seen in Fig. 11. Before failure, presumably cracks are well dispersed and do not grow sufficiently large to intersect with neighboring cracks minimizing any deviations from brittle-like behavior. For elastic-plastic binders, the number of cracks also rises with strain in both the strongly- and weakly-adhered systems, however, a peak followed by a significant decay in the number of cracks is only seen at large P.

In many continuum models, the primary quantity of interest is a length scale of a crack as in the viscoSCRAM model [35]. Therefore, for each set of broken bonds in a crack, we find the minimum bounding box, mapping across

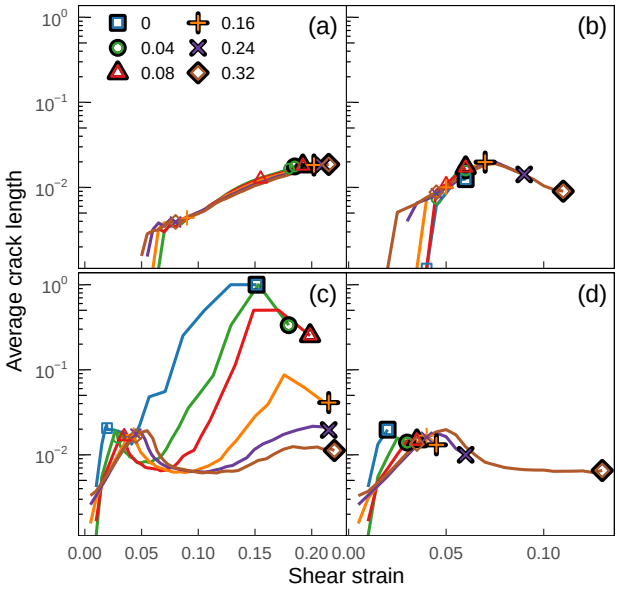

Figure 13: Average length of cracks in the system normalized by $200\sqrt{3}d$, the maximum length scale in the undeformed system. Symbols indicate approximate locations of yield (no outline) and failure (black outline) within an accuracy of 0.5% strain. Systems correspond to the (a) elastic/strong, (b) elastic-plastic/strong, (c) elastic/weak, and (d) elastic-plastic/weak binder models listed in Table 1.

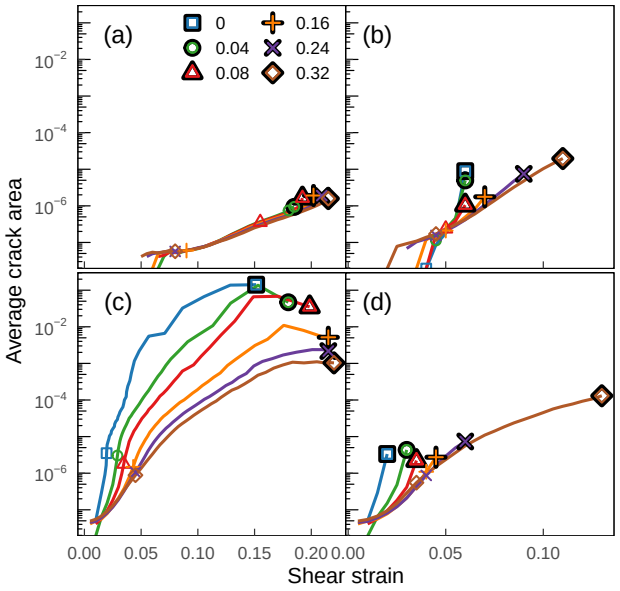

Figure 14: The average area of a crack quantified by the number of broken bonds in a crack as a function of strain. The average area is normalized by the total number of binder bonds, $\sim 5 \times 10^7$. Symbols indicate approximate locations of yield (no outline) and failure (black outline) within an accuracy of 0.5% strain. Systems correspond to the (a) elastic/strong, (b) elastic-plastic/strong, (c) elastic/weak, and (d) elastic-plastic/weak binder models listed in Table 1.

periodic boundaries as necessary, and estimate length of the crack as the maximum diagonal distance across the box. During shear, large clusters of broken bonds will eventually span the entire system as systems fracture. Due to periodic boundary conditions, defining the length of these percolating cracks (which may or may not self-intersect across a period boundary) is ambiguous so we simply cap the maximum length of a crack at $200\sqrt{3}d$, the maximum distance across the initial system. Using this definition, the average length of a crack normalized by this maximum allowed crack length is plotted in Fig. 13.

As expected, the average normalized crack length initially grows in all systems at small strains. In the elastic/strong case, this growth continues up until failure. The average never grows very large due to the presence of many small cracks seen in Fig. 11. In other cases, this metric peaks and then slightly decays before, in some instances, rising again. This decrease is not caused by an increase in the number of small cracks as it coincides with a reduction in the total number of cracks. Alternatively, this effect appears to be due to the coalescence of larger cracks. Unless cracks are aligned on a plane, the length of the coalesced pair is less than the sum of their initial lengths. This causes an apparent reduction in the average crack length as a consequence of defining length using a minimum-bounding-box. Once a crack spans the diagonal of the system, no amount of coalescence will increase its length.

This effect is fundamentally a restriction from reducing a crack to a linear measure: it neglects that cracks have a length and a width and can branch through a complex heterogeneous system. Therefore, we also calculate the number of broken bonds in a crack which, for simple geometries, will be proportional to the total area of a crack. This metric will combine additively as cracks coalesce. The average area of a crack using this definition, plotted in Fig. 14, generally grows with strain in all systems. As before, the finite system size places a maximum limit on the area of a crack as the total number of bonds that can break in the binder or $\sim 5 \times 10^7$. This limit is used as a normalization. Note that in this extreme limit where a crack constitutes nearly all of the bonds in the binder, this definition will no longer correspond to an area so the terminology is not perfect.

Using either metric, one can identify a few important results. First and foremost is that pressure does generally suppress crack growth in all cases except for the elastic/strong case. At small pressures, the average crack length and area tend to grow faster with increasing strain, leading to failure. This is reinforced by the finding from the previous section that bond breakage is more prevalent at lower mean pressures, while higher pressures generally limit the number of bonds that break with shear. Secondly in systems with elastic-plastic binders, Figs. 13 and 14 suggest there may be some standard, pressure-independent evolution of the average length and area of cracks that extends to larger strains with increasing P. Lastly in the elastic/weak case, very large cracks are observed before

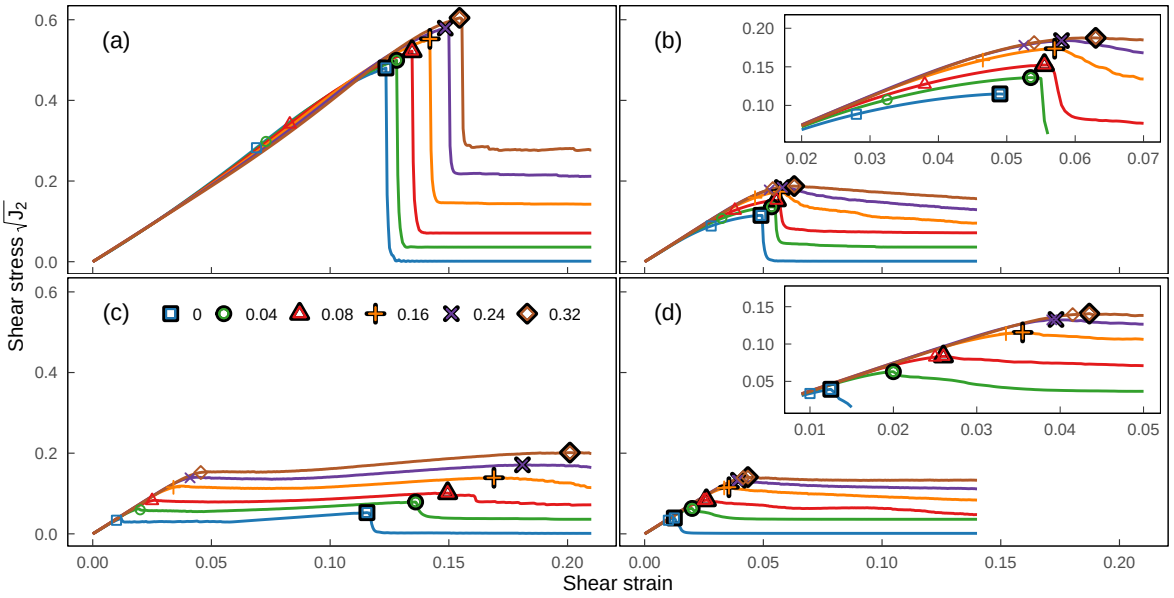

Figure 15: Example stress-strain curves in TXE. Symbols indicate locations of yield (no outline) and failure (black outline). Systems correspond to the (a) elastic/strong, (b) elastic-plastic/strong, (c) elastic/weak, and (d) elastic-plastic/weak binder models listed in Table 1.

failure. These are clusters of filler grain surfaces that have separated from the binder seen in Fig. 8 which constitute a significant portion of the system.

Of course, this mesoscopic dataset provides far more information than the brief analysis provided in this section as one has access to the full evolution of crack size distributions with strain. These time-dependent distributions also contain information on the rate of crack growth and coalescence as a function of crack sizes. Finally, cracks have complex orientations and shapes which may provide more predictive information than simple scalar metrics of size. This may be particularly relevant given the anisotropic treatment of damage evolution in many macroscale models [4].

In future work, similar datasets will be a valuable tool to test various metrics describing crack evolution and identify which are most valuable to continuum damage formulations and failure criteria. Such studies will augment the many existing finite-element-based mesoscale models, and the relatively few experimental datasets that contain detailed mesoscopic information. As many finite element-based studies use cohesive zones to represent cracking along filler-binder interfaces [40, 26, 52] but include no mechanisms for localized ruptures within the binder, comparisons could provide useful insights on the role of binder behavior that will be important to include in future models and can guide new experiment designs. Additionally, since mesoscale crack evolution may play a prevalent role in hot spot formation under higher strain rate loadings [37, 36], further studies should also explore ways to quantify the energy dissipation pathways associated with crack nucleation and growth.

3.4. Dependence on Lode Angle

The mechanical response of a material often depends on the Lode angle of deformation. Accurate predictions of the performance of highly filled polymer composites in arbitrary environments therefore require insight into the relevance of different physical mechanisms at different Lode angles. Despite the impact Lode angle has on performance, such information is unfortunately scarce [4]. In this section, we model the strength of granular composites under triaxial extension (TXE) to identify qualitative differences in the mechanical response and quantify relative differences from TXC.

In Fig. 15, stress-strain curves under TXE loading generally resembles those found in TXC, however, there are a few key differences. In the elastic/strong case (Fig. 15[a]), curves still well-approximate a brittle system. However, as opposed to becoming slightly less stiff with strain as seen in TXC, the system becomes slightly stiffer. The slight pressure-dependent splay in curves then inverts the relation between yield and pressure. Systems at low P yield earlier in TXE. In the elastic/weak scenario (Fig. 15[c]), a strain-hardening regime still appears at all pressures but is less pronounced than in TXC. Furthermore, the strain-softening regime at low mean pressures almost disappears. In the elastic-plastic/strong case (Fig. 15[b]), yield has a considerably stronger dependence on P creating a larger splay between curves before failure. Failure also occurs in a narrower window of strain across pressures compared to TXC. In the elastic-plastic/weak system (Fig. 15[d]), strain-hardening is no longer seen as failure quickly follows yield at all P.

These changes between TXC and TXE in the shape of stress-strain curves suggests there are fundamental shifts

in microscopic behavior. While a complete dissection of these phenomena is beyond the scope of this work, the evolution of microscopic properties under TXE is briefly explored in Appendix B. This data exhibits important qualitative differences between TXE from TXC. To quantify the relative importance of Lode angle, the ratios of the yield and peak stresses averaged across the five RVs under TXE relative to TXC are plotted as a function of pressure for the four material property cases in Fig. 16. Unsurprisingly, yield in the elastic/strong case exhibits a strong dependence on Lode angle that varies considerably with pressure. As the location of yield in this case is highly sensitive to the definition, the error bars may not accurately convey uncertainty so we avoid drawing conclusions on this data.

In the other three cases, we find the ratio of yield stresses in TXE relative to TXC increases almost linearly with P. Thus, the ratio crosses unity as the yield stress is higher in TXC at low pressures but becomes larger in TXE at high pressures. This observation highlights a novel dependence on Lode angle that would have repercussions in designing an accurate continuum model. We note that the yield discussed here, refers to the yield stress extracted from the shear stress-shear strain curves at the end of the linear regime (see Subsec. 3.1). This is not necessarily analogous to the onset of permanent, plastic deformation defined by a traditional yield surface, as the inelastic damage mechanisms that reduce material stiffness also contribute to loss of linearity in the stress-strain curve. Without further simulations that include both loading and unloading, it is impossible to differentiate the onset of these two phenomena and determine which is driving the unique anisotropic behavior presented here. However, what is clear is that the combination of these two mechanisms results in a marked tension-compression asymmetry, which is consistent with observations of various PBX materials in the literature [4]. An additional contribution of this work is to demonstrate that this tension-compression asymmetry also depends strongly on confining pressure for all binder and grain-binder interface properties studied here. These results suggests that both the damage formulation and the plastic yield surface in continuum models should consider anisotropic dependence on Lode angle and the mean pressure, and that a comprehensive suite of tests in multi-axial stress states is necessary to fully characterize a particular material's behavior.

The ratio of peak stresses in TXE to TXC, which we refer to as the failure strength ratio, can be thought of as a measure of the importance of Lode angle on the material's ultimate strength. The failure strength ratio is expected to be less than or equal to unity and is often used when calibrating failure surface models [53]. A failure strength ratio of unity suggests the material's strength does not depend on the direction of shear such that a Drucker-Prager failure surface (a circle on a π plane) is a reasonable approximation. However, we find that the strength ratio in Fig. 16(b) is always less than one implying TXC always exhibits a higher peak stress. This data implies that a Drucker-Prager failure surface never correctly describes behavior in these simulations since failure always has some dependence on Lode angle or the J_3 invariant [54]. However the data in Fig. 16(b) is insufficient to suggest an alternative choice. Further study of this topic is clearly needed.

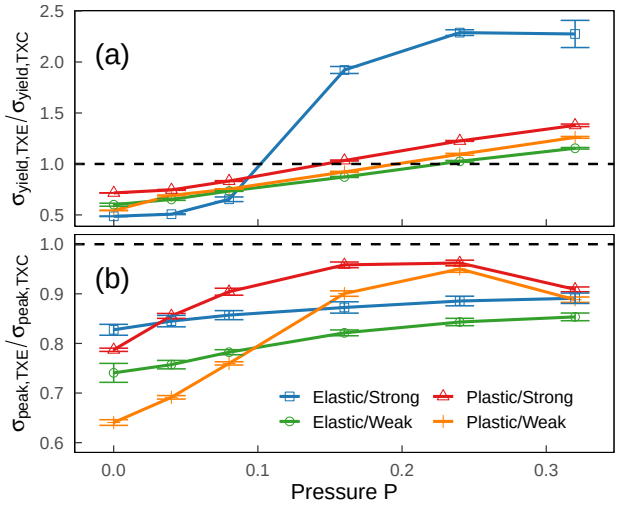

Figure 16: Ratio of (a) the average yield stress and (b) the average peak stress between TXE to TXC as a function of pressure for the indicated systems.

When studying the pressure dependence of the failure strength ratio, a monotonic increase is observed with increasing pressure in systems with elastic binders. This suggests Drucker-Prager will become a more accurate approximation (although still insufficient) with increasing pressure as systems display a softer dependence on Lode angle. For plastic binders, an interesting non-monotonic trend is seen in both cases where the failure strength ratio initially increases before peaking and dropping at higher pressure - possibly due to a less substantial strain-hardening regime at high pressures in TXE relative to TXC. This behavior is unusual, and its origin will need to be explored in future work.

Although this brief investigation only scratched the surface of various multiaxial stress states, it unveiled a wide array of behavioral changes that has significant ramifications on continuum constitutive model development for highly filled polymer bound granular composites. Not only does the failure strength exhibit tension-compression asymmetry under all binder properties and pressures, but the shape of stress-strain curves also varies exhibiting yield stresses that depend on Lode angle. These findings further motivate the need for both experimental and computational studies of polymer bonded composite materials that systematically vary Lode angle as argued in Ref. [4].

4. Summary and Outlook

Polymer bonded granular composites constitute a wide range of materials and have many applications which require predictive modeling capability of their mechanical response, such as the safety of energetic components. Due to their complex, heterogeneous structure, the development of predictive models is a challenge as the mechanical response depends on the interaction of multiple physical mechanisms which further depend on the loading history and stress state of the system. In this work, we leveraged the flexibility and fully exposed dynamics of BPM simulations to probe the behavior of sheared polymer bonded granular composites at varying pressures, binder constitutive behaviors, and grain-binder interface strengths. Key findings of this approach include:

- Using a bonded particle model gave flexibility to easily study abstract changes in material properties or loading conditions through simple changes in the bond force model. Computationally efficient simulations of large systems can also provide access to information across length scales: macroscopic behavior of a representative volume, mesoscopic damage and crack growth on the length scale of grains, and microscopic activation of inelastic mechanisms at the subgrain resolution of particles.

- Two different models of binder-binder bond properties were used to approximate the behavior seen in polymers: 1) well below their glass transition temperature (elastic-plastic binder bonds) and 2) well above their glass transition temperature (elastic bonds). These two cases represent limiting scenarios that a polymer bonded energetic material may see if loaded across a wide temperature range during its lifetime. Two different sets of filler grain-binder bond properties were also used to explore the limiting cases of "weak" and "strong" interfacial adhesive strengths.

- Increasing the confining pressure generally strengthens the material in all cases. It also introduces many other changes in the mechanical response. Examples seen here include transition from a strain-softening regime to a strain-hardening regime in the elastic/weak case, lengthening of strain-hardening regime to larger strains in the elastic-plastic/strong case, and less brittle failure in the elastic-plastic/weak case.

- While not a direct representation of any specific material formulation, the findings of this study are consistent with trixial test data for PBX materials loaded both above (EDC37 [13]) and below (M2 [4]) their glass transition temperatures. We show that both binder and binder-grain interface properties strongly affect the pressure-dependent response of such materials.

- We know that yield and the emergence of strain-softening/hardening regimes in the mechanical response of polymer bonded composites is due to inelastic mechanisms in the material that are different than the dislocation-based plasticity characteristic of metals. By considering the global RV response and concurrently tracking the microscopic activation of the available inelastic mechanisms in our simulations (broken bonds or binder plasticity), we can begin to probe these linkages between microstructure evolution and macroscale mechanical behavior.

- By considering the spatial correlations of broken bonds, one can aggregate this data into cracks and acquire more insight into the damage accumulation and failure of these materials. Different crack descriptor metrics can produce very different results. However, further work is needed to determine the most useful quantities to inform continuum damage and failure models.

- Material yield and ultimate failure strength can vary up to $\sim$ 40% with the Lode angle depending on the confining pressure and material properties. The strain at which yield occurs also changes significantly when comparing triaxial extension (TXE) to triaxial compression (TXC). Yield occurs later in TXE at low pressures but later in TXC at high pressures. This behavior is likely emergent from the complex interplay between the various inelastic mechanisms at the mesoscale, which are affected by the increase in confining pressure.

- Consideration of these pressure-dependent behaviors is necessary for continuum models to be predictive in arbitrary, complex loading scenarios. Correspondingly, standard material characterization paradigms should include tests that probe multiaxial stress states (e.g. triaxial compression, channel die tests, equibiaxial tests) at a variety of hydrostatic pressure conditions.

While these results begin to address the dearth of information on what drives the mechanics of these complex composites, there is far more that should be considered in future studies. For instance, these simulations have a relatively high fraction of binder as a consequence of the monodisperse, spherical grains. The effect of filler grain morphological factors including polydispersity and asphericity, which can lead to the denser packings that are seen in many PBX materials, are as yet unexplored. Furthermore, only the two extreme Lode angles were tested here providing insufficient data to identify potential failure surface models that could be implemented in a continuum description. Our brief analysis of mesoscopic dynamics clearly illustrates the complex micromechanical interactions that govern the macroscale material response, but merely scratched the surface of information that could

be used to inform macroscopic damage models and failure criteria. Nonetheless, the findings shown here clearly demonstrate the importance of confining pressure on the mechanical response of polymer bonded granular composites across a wide range of binder and grain-binder interface behaviors relevant to energetic materials. We hope that both the conclusions drawn and questions raised in this work continue to drive future research on their mechanical behavior under multiaxial stress states.

5. Acknowledgments

The authors acknowledge Bill Erikson and Chet Vignes for their helpful review and discussions, and Jeremy Lechman and Stacy Nelson for management support.

This work is funded by Sandia's Laboratory Directed Research and Development program. This article has been authored by an employee of National Technology & Engineering Solutions of Sandia, LLC under Contract No. DE-NA0003525 with the U.S. Department of Energy (DOE). The employee owns all right, title and interest in and to the article and is solely responsible for its contents. The United States Government retains and the publisher, by accepting the article for publication, acknowledges that the United States Government retains a non-exclusive, paid-up, irrevocable, world-wide license to publish or reproduce the published form of this article or allow others to do so, for United States Government purposes. The DOE will provide public access to these results of federally sponsored research in accordance with the DOE Public Access Plan https://www.energy.gov/downloads/doe-public-access-plan. This paper describes objective technical results and analysis. Any subjective views or opinions that might be expressed in the paper do not necessarily represent the views of the U.S. Department of Energy or the United States Government.

Appendix A. Representative Volume Convergence Assessments

As we extract homogenized (volume averaged) stress and strain invariants of the representative volumes (RV) [55], we must establish that the RVs are large enough such that our volume averaged results are independent of RV size [56]. First, we show that fluctuations in volume fraction with respect to larger subdomain sampling has converged with respect to the mean filler volume fraction. This establishes that the filler volume fraction is size converged for the RVs. Then, we examine properties of the filler-particle phase autocorrelation and establish that the RVs are isotropic. With these results in hand, we examine the collection of stress invariant responses from all five RVs together for select material property cases and establish that fluctuations in the mechanical response are very small across the five RVs and finally test convergence with the number of particles in a system.

The five RVs studies are two phase structures of monodisperse spherical filler grains in an otherwise uniform binder with a filler volume fraction near 64%. Each RV is voxellated into 200 x 200 x 200 cells taking for each cell the material identification, 1 for the filler or 0 for the binder at the centroid of the cell. Slices about the midplane of the voxellated first RV are shown in Fig. A.17 demonstrating that the voxel resolution is sufficient.

To establish that the RVs are size converged with respect to first order metrics such as volume fractions, we compute the density coarseness measure [57]. Here, progressively larger and larger subdomains starting at 2 x 2 x 2 (1% of the RV edge length on a subdomain window side) and ending at 32 x 32 x 32 (16% of the RV edge length on a subdomain side) voxels are considered. The filler volume fraction and its standard of deviation are computed on a 1000 random subdomains for each of the subdomain sizes. We plot this density coarseness measure in Fig. A.18, which indicates that the filler volume fraction converges statistically quickly with RV size, and that our RVs do not fluctuate in filler volume fraction. Note that this analysis does not address the related question of whether results are converged in terms of the number of particles. In other words, whether a sufficient number of particles are used to resolve the mesostructure. This analysis is discussed at the end of this appendix.

Next, we seek to establish if our mesostructures are isotropic. We compute the filler-filler spatial autocorrelation. Slices of that autocorrelation for the representative RV number one are shown in Fig. A.19. The other four RVs exhibit nearly identical filler-filler spatial autocorrelations by eye. To establish isotropy, we plot rays of the filler-filler autocorrelations in each Cartesian direction and compare the autocorrelation value against autocorrelation distance in Fig. A.20. These results establish that the autocorrelations along the three Cartesian axes are similar across directions and RVs which establishes no statistical preference in filler spatial layout along these three directions.

Next, we demonstrate that the five RVs exhibit minimal fluctuations in their mechanical response to shear. Average stress-strain curves are calculated using data from the five RVs and plotted in Fig. A.21. At every instance of strain, the standard deviation is indicated using a lightly filled area. The response of the five RVs are extremely consistent with minimal variations in the mechanical response up until failure. All RVs exhibit the same loading regimes discussed in Subsec. 3.1. At failure, there is some deviation between curves as the exact location of failure depends on the specific RV (particularly when the system fails in a brittle manner). Despite this splay, the peak stresses of the five RVs are still quite similar as indicated by the error bars in Figs. 5 and 16. After failure, RVs may diverge which is not surprising as the exact path of cracks will depend on the locations of grains introducing variation in the structure and surface morphology of the fractured system.

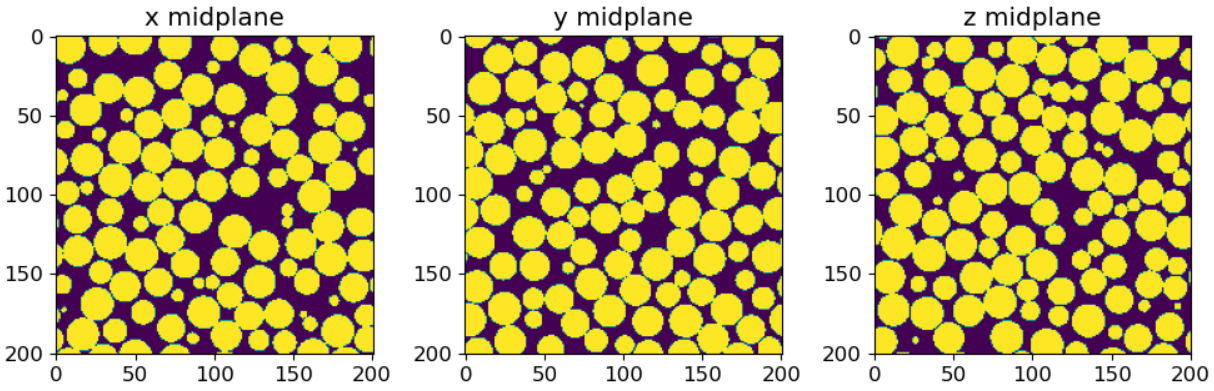

Figure A.17: Representative volume RV1 voxellated into 200 x 200 x 200 cells. Slices of the mesostructure are shown looking along the three Cartesian directions at its center. The additional RVs (RV2-RV5) are qualitatively similar.

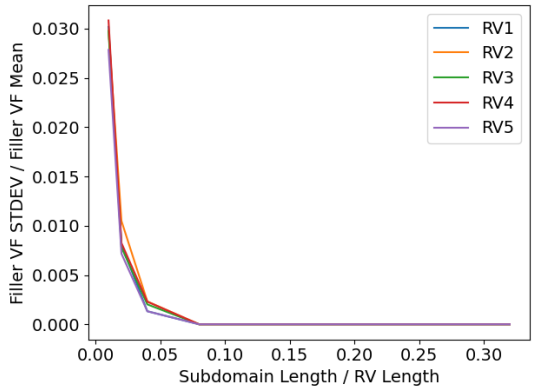

Figure A.18: Filler volume fraction coarseness measure demonstrates that the volume fraction does not fluctuate beyond a fraction of the RV sizes considered in this work.

Finally, we consider the related problem of whether our simulations are converged in terms of resolution. On other words, are enough simulation particles used to represent the mesostructure of a given RV. In Fig. A.22, stress-strain curves are included for different resolutions at zero mean pressure. The value in the legend corresponds to the diameter of the filler grains in units of d, i.e. the number of particle diameters that span a grain diameter. At the lowest resolution, $2.6125d$, the system has a total of $\sim 150,000$ particles (or around 100 particles per grain) while at the highest resolution, $10.5d$, the system has almost 10 million particles. This maximum resolution was used for all other results in this paper. Higher resolutions were not tested due to the increased computational costs. In all cases, failure occurs earlier with increasing resolution. However, curves appear to be converging and differences between the two highest resolutions are relatively minor and the same strain-softening and -hardening regimes are still seen at lower resolutions. Therefore, we expect minimal error due to the finite resolution of the mesostructure in terms of particles.

Appendix B. Microscopic Results in TXE

In Subsection 3.4, the impact of Lode angle was briefly touched upon by studying stress-strain curves under triaxial extension (TXE). Some notable differences were found in the shape of curves as well as the yield and peak stresses. In this appendix, we briefly look at the evolution of microscopic quantities as a function of shear to provide some initial context on which quantities may be relevant to changes in the mechanical response. However, identifying concrete links between changes in the macroscopic and microscopic behavior in TXE is beyond the scope of this work.

In Subsection 3.2, we considered two primary measure of inelastic activity in TXC: the fraction of broken bonds and the fraction of plastically deformed bonds in the binder. The fraction of broken bonds is plotted versus strain in Fig. B.23, the TXE equivalent to Fig. 7. While most data is qualitatively similar, we identify two primary differences. First in the elastic/strong system, the fraction of broken binder-binder and binder-grain bonds displays a significantly stronger dependence on pressure. The increase in the number of broken bonds is delayed with increasing pressure. In TXC, little pressure dependence was seen (Fig. 7[a]). Secondly in the elastic/weak system, there is a notable reduction in the rate at which binder-grain bonds break with strain under low confinement. This behavior may be linked to the diminished strain-softening regime at low P in Fig. 15(c). Furthermore, curves saturate at a slightly lower value such that a non-negligible number of interfacial bonds survive up to failure.

While there are no stark differences between the rate of bond breakage in elastic-plastic binders under TXE relative to TXC, differences are apparent in the fraction of plastically active bonds seen in Fig. B.24. With both strong and weak interfacial bonds, the onset of plasticity has a larger dependence on pressure in TXE than TXC (Fig. B.24[a] and [c]). This may be connected to the larger strain-hardening regimes seen in the elastic-plastic/strong case under TXE. Additionally in the well-adhered case, the fraction of plastic bonds that break displays an inverted

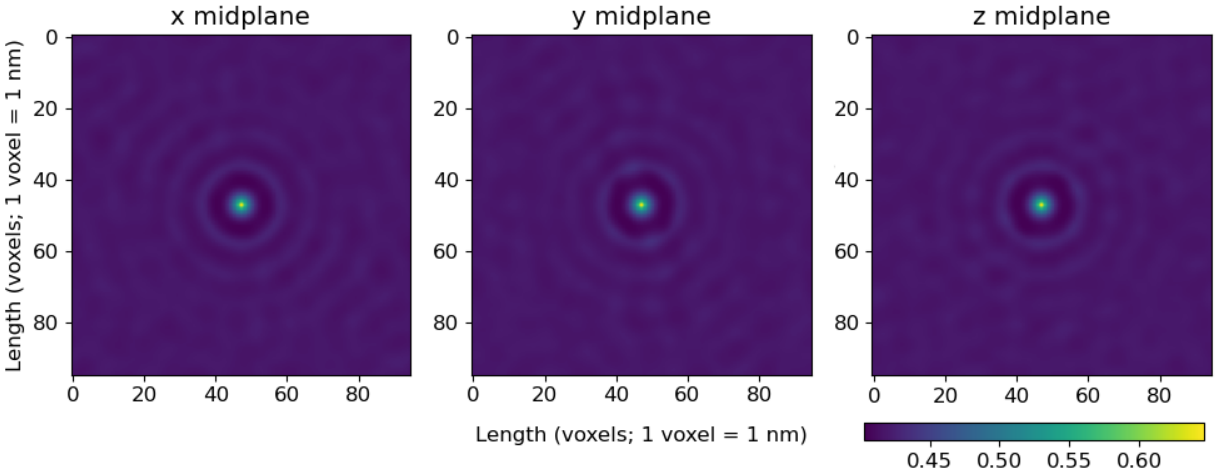

Figure A.19: Slices about the center of the filler-filler spatial autocorrelation for RV1. The other RVs are qualitatively similar.

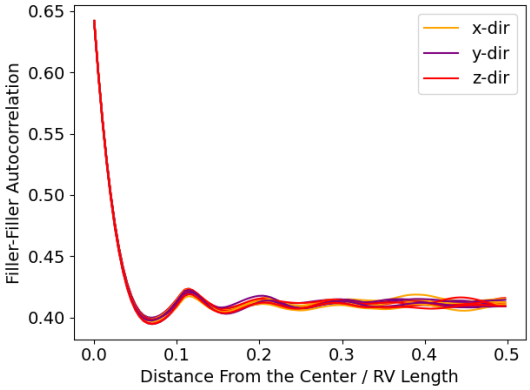

Figure A.20: Rays along the three Cartesian directions of the filler-filler spatial autocorrelations for each of the five RVs.

trend with pressure. Instead of having a higher fraction of plastic bonds break at higher P in TXC seen in Fig. 9(b), in TXE a higher fraction is seen at lower P.

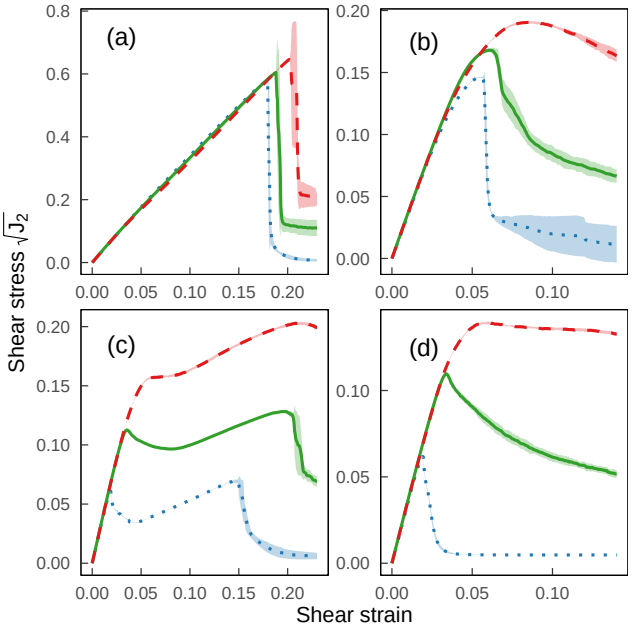

Figure A.21: Stress strain curves averaged across five mesostructure realizations, or RVs, in TXC at pressures of 0 (dotted, blue), 0.08 (solid, green), and 0.24 (dashed, red) for the (a) elastic/strong, (b) elastic-plastic/strong, (c) elastic/weak, and (d) elastic-plastic/weak models. Ribbons correspond to one standard deviation and only become significant around failure.

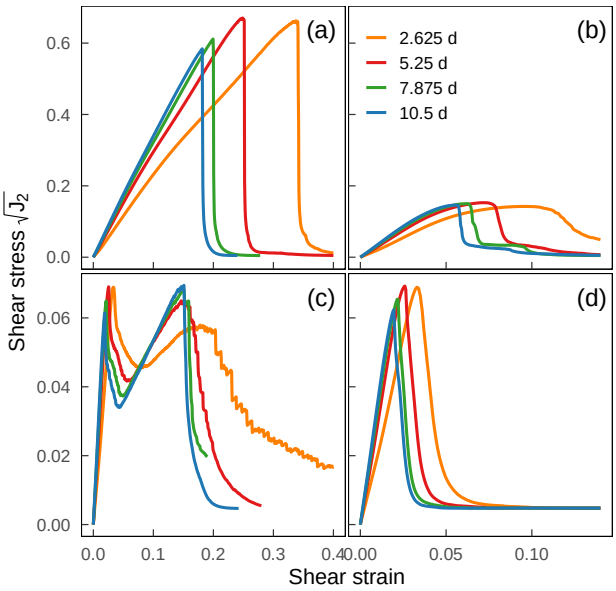

Figure A.22: Stress strain curves at $P = 0$ in TXC at the indicated resolution for the (a) elastic/strong, (b) elastic-plastic/strong, (c) elastic/weak, and (d) elastic-plastic/weak models.

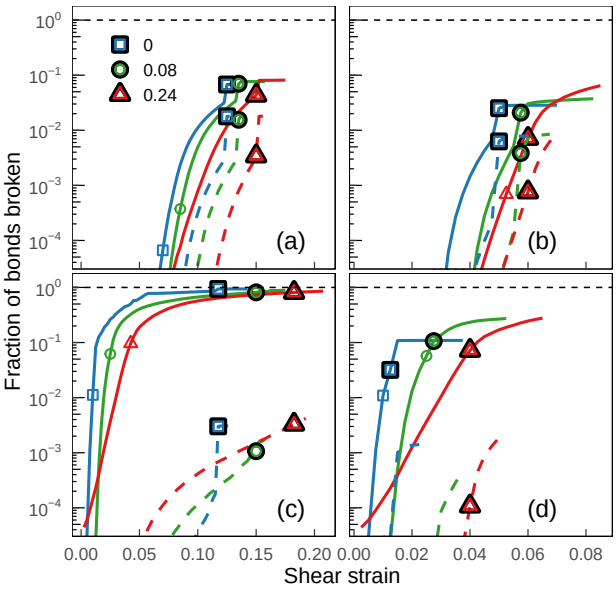

Figure B.23: Fraction of interfacial binder-grain (solid lines) and binder-binder (dashed lines) bonds broken as a function of strain at the indicated pressures under TXE. Symbols indicate approximate locations of yield and failure to within an accuracy of 0.25% strain. The dashed line represents 100% of bonds broke. Data is truncated at a fraction of 5×10^{-5}. Systems correspond to the (a) elastic/strong, (b) elastic-plastic/strong, (c) elastic/weak, and (d) elastic-plastic/weak binder models listed in Table 1.

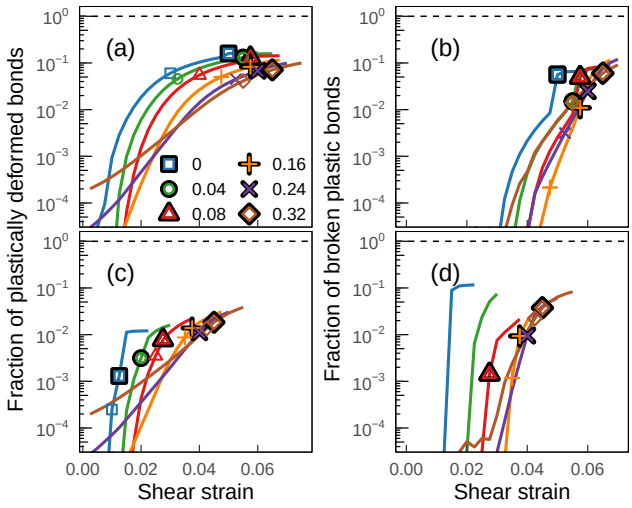

Figure B.24: (a,c) Fraction of binder bonds that have plastically deformed by reaching a strain of 5% as a function of shear strain at the indicated pressures in TXE. (b,d) The fraction of these plastically activated bonds that broke versus shear strain. Data in the top row corresponds to the (a,b) elastic-plastic/strong case and in the bottom row (c,d) to the elastic-plastic/weak case. Symbols representing yield (no outline) and peak stress (black outline) are placed with an accuracy of 0.25% strain. Data is truncated at fractions of 5×10^{-5}. The horizontal dashed line represents 100%.

References

[1] M. K. Neilsen, K. N. Austin, D. B. Adolf, S. W. Spangler, M. A. Neidigk, R. S. Chambers, Packaging strategies for printed circuit board components. volume i, materials and thermal stresses. (9 2011). doi:10.2172/1022184.
URL https://www.osti.gov/biblio/1022184

[2] J. E. Kennedy, Impact and Shear Ignition By Nonshock Mechanisms, Springer Berlin Heidelberg, Berlin, Heidelberg, 2010, pp. 555–581. doi:10.1007/978-3-540-87953-4_10.
URL https://doi.org/10.1007/978-3-540-87953-4_10

[3] C. M. Tarver, S. K. Chidester, On the violence of high explosive reactions, Journal of Pressure Vessel Technology 127 (1) (2005) 39–48. arXiv:https://asmedigitalcollection.asme.org/pressurevesseltech/article-pdf/127/1/39/5573439/39_1.pdf, doi:10.1115/1.1845474.
URL https://doi.org/10.1115/1.1845474

[4] G. Plassart, D. Picart, M. Gratton, A. Frachon, M. Caliez, Quasistatic mechanical behavior of hmx- and tatb-based plastic-bonded explosives, Mechanics of Materials 150 (2020) 103561. doi:https://doi.org/10.1016/j.mechmat.2020.103561.
URL https://www.sciencedirect.com/science/article/pii/S0167663620306037

[5] D. A. Wiegand, B. Reddingius, Mechanical properties of confined explosives, Journal of Energetic Materials 23 (2) (2005) 75–98. arXiv:https://doi.org/10.1080/07370650590936415, doi:10.1080/07370650590936415.
URL https://doi.org/10.1080/07370650590936415

[6] W. R. Blumenthal, D. Thompson, C. M. Cady, G. T. Gray III, D. J. Idar, Compressive properties of pbxn-110 and its htpb-based binder as a function of temperature and strain rate, Tech. Rep. LA-UR-02-3183, Los Alamos National Laboratory (August 2002).

[7] E. Duncan, J. Margetson, A nonlinear viscoelastic theory for solid rocket propellants based on a cumulative damage approach, Propellants, Explosives, Pyrotechnics 23 (2) (1998) 94–104.

[8] J. Xu, X. Chen, H. Wang, J. Zheng, C. Zhou, Thermo-damage-viscoelastic constitutive model of htpb composite propellant,

International Journal of Solids and Structures 51 (18) (2014) 3209 – 3217. doi:https://doi.org/10.1016/j.ijsolstr.2014.05.024.
URL http://www.sciencedirect.com/science/article/pii/S0020768314002182

[9] M. Gratton, C. Gontier, S. Rja Fi Allah, A. Bouchou, D. Picart, Mechanical characterisation of a viscoplastic material sensitive to hydrostatic pressure, European Journal of Mechanics - A/Solids 28 (5) (2009) 935–947. doi:https://doi.org/10.1016/j.euromechsol.2009.03.002.
URL https://www.sciencedirect.com/science/article/pii/S0997753809000345

[10] C. Gruau, D. Picart, R. Belmas, E. Bouton, F. Delmaire-Sizes, J. Sabatier, H. Trumel, Ignition of a confined high explosive under low velocity impact, International Journal of Impact Engineering 36 (4) (2009) 537–550. doi:https://doi.org/10.1016/j.ijimpeng.2008.08.002.
URL https://www.sciencedirect.com/science/article/pii/S0734743X08002182

[11] P. Ragaswamy, M. W. Lewis, C. Liu, D. G. Thompson, Modeling the mechanical response of pbx 9501, in: Proceedings of the Fourteenth International Detonation Symposium, 2010, pp. 174–183.

[12] V. D. Le, M. Gratton, M. Caliez, A. Frachon, D. Picart, Experimental mechanical characterization of plastic-bonded explosives, Journal of Materials Science 45 (2010) 5802–5813. doi:10.1007/s10853-010-4655-5.
URL https://doi.org/10.1007/s10853-010-4655-5

[13] D. A. Wiegand, B. Redingius, K. Ellis, C. Leppard, Pressure and friction dependent mechanical strength – cracks and plastic flow, International Journal of Solids and Structures 48 (11) (2011) 1617–1629. doi:https://doi.org/10.1016/j.ijsolstr.2011.01.025.
URL https://www.sciencedirect.com/science/article/pii/S0020768311000424

[14] D. Picart, J. Ermisse, M. Biessy, E. Bouton, H. Trumel, Modeling and simulation of plastic-bonded explosive mechanical initiation, International Journal of Energetic Materials and Chemical Propulsion 12 (6) (2013) 487–509.

[15] M. Chatti, A. Frachon, M. Gratton, M. Caliez, F. Lacroix, D. Picart, N. A. Hocine, Experimental investigation of multiaxial failure and identification of failure criteria for a pbx simulant material, International Journal of Energetic Materials and Chemical Propulsion 20 (2) (2021) 87–108.

[16] V. W. Manner, J. D. Yeager, B. M. Patterson, D. J. Walters, J. A. Stull, N. L. Cordes, D. J. Luscher, K. C. Henderson, A. M. Schmalzer, B. C. Tappan, In situ imaging during compression of plastic bonded explosives for damage modeling., Materials (Basel) 10 (6) (Jun 2017). doi:10.3390/ma10060638.

[17] P. J. Rae, S. J. P. Palmer, H. T. Goldrein, J. E. Field, A. L. Lewis, Quasi-static studies of the deformation and failure of pbx 9501, Proceedings: Mathematical, Physical and Engineering Sciences 458 (2025) (2002) 2227–2242.
URL http://www.jstor.org/stable/3067368

[18] P. Chen, H. Xie, F. Huang, T. Huang, Y. Ding, Deformation and failure of polymer bonded explosives under diametric compression test, Polymer Testing 25 (3) (2006) 333 – 341. doi:https://doi.org/10.1016/j.polymertesting.2005.12.006.
URL http://www.sciencedirect.com/science/article/pii/S0142941806000080

[19] S. J. P. Palmer, J. E. Field, J. M. Huntley, Deformation, strengths and strains to failure of polymer bonded explosives, Proceedings: Mathematical and Physical Sciences 440 (1909) (1993) 399–419.
URL http://www.jstor.org/stable/52242

[20] Z. Hu, H. Luo, S. Bardenhagen, C. Siviour, R. Armstrong, H. Lu, Internal deformation measurement of polymer bonded sugar in compression by digital volume correlation of in-situ tomography, Experimental Mechanics 55 (2015) 289–300.

[21] D. M. Wood, Soil behaviour and critical state soil mechanics, Cambridge university press, 1990.

[22] M. A. Buechler, Viscoelastic-viscoplastic combined hardening constitutive model based on the drucker prager yield and flow potentials, Tech. Rep. LA-UR-12-24895, Los Alamos National Laboratory (September 2012).

[23] M. A. Buechler, Viscoelastic viscoplastic damage model development, parameter estimation, and comparison to pbx9501 experimental data, Tech. Rep. LA-UR-13-27547, Los Alamos National Laboratory (September 2013).

[24] P. Kakavas, Mechanical properties of propellant composite materials reinforced with ammonium perchlorate particles, International Journal of Solids and Structures 51 (10) (2014) 2019 – 2026. doi:https://doi.org/10.1016/j.ijsolstr.2014.02.015.
URL http://www.sciencedirect.com/science/article/pii/S0020768314000638

[25] J. Brown, F. Beckwith, K. Wolf, M. Cooper, C. Vignes, K. Long, The role of pressure-dependent plasticity and volumetric dilitation in energetic materials at intermediate strain rates, R. Soc. Chem. Proc. (2023).

[26] D. J. Walters, D. J. Luscher, J. D. Yeager, B. M. Patterson, Cohesive finite element modeling of the delamination of htpb binder and hmx crystals under tensile loading, International Journal of Mechanical Sciences 140 (2018) 151–162.

[27] J. E. Reaugh, B. W. White, J. P. Curtis, H. K. Springer, A computer model to study the response of energetic materials to a range of dynamic loads, Propellants, Explosives, Pyrotechnics 43 (2018) 703–720.

[28] J. Li, F. Lu, J. Qin, R. Chen, P. Zhao, L. Lan, S. Jing, Effects of temperature and strain rate on the dynamic responses of three polymer-bonded explosives, The Journal of Strain Analysis for Engineering Design 47 (2) (2012) 104–112. arXiv:https://doi.org/10.1177/0309324711428836, doi:10.1177/0309324711428836.
URL https://doi.org/10.1177/0309324711428836

[29] R. Stevens, A strength model and service envelope for pbx 9501, Tech. Rep. LA-UR-14-20696, Los Alamos National Laboratory (February 2014).

[30] Q. Wei, X. cheng Huang, P. wan Chen, R. Liu, A pressure-dependent plasticity model for polymer bonded explosives under confined conditions, Central European Journal of Energetic Materials 18 (3) (2021) 339–368. doi:10.22211/cejem/142512.
URL https://ipo.lukasiewicz.gov.pl/wydawnictwa/cejem-woluminy/vol-18-nr-3/

[31] M. Liu, X. Huang, Y. Wu, C. Chen, F. Huang, Numerical simulations of the damage evolution for plastic-bonded explosives subjected to complex stress states, Mechanics of Materials 139 (2019) 103179. doi:https://doi.org/10.1016/j.mechmat.2019.103179.
URL https://www.sciencedirect.com/science/article/pii/S0167663619304120

[32] M. Liu, X. Huang, Y. Wu, F. Huang, C. Liu, Modeling of the deformation and damage of plastic-bonded explosive in consideration of pressure and strain rate effects, International Journal of Impact Engineering 146 (2020) 103722. doi:https://doi.org/10.1016/j.ijimpeng.2020.103722.
URL https://www.sciencedirect.com/science/article/pii/S0734743X20307922

[33] G. Kalsi, Experimental characterisation and modelling of the mechanical behaviour of polymer-bonded explosives, in: Proceedings of the NAFEMS World Congress 2011, Boston, MA, 2011.

[34] G. Kalsi, On the experiences of adding a complex user-material-model to ls-dyna, in: 12th International LS-DYNA Users Conference, 12th International LS-DYNA Users Conference, Detroit, MI, 2012.

[35] M. A. Buechler, D. J. Luscher, A semi-implicit integration scheme for a combined viscoelastic-damage model of plastic bonded explosives, International Journal for Numerical Methods in Engineering 99 (1) (2014) 54–78.

[36] A. Keyhani, S. Kim, Y. Horie, M. Zhou, Energy dissipation in polymer-bonded explosives with various levels of constituent

plasticity and internal friction, Computational Materials Science 159 (2019) 136 – 149. doi:https://doi.org/10.1016/j.commatsci.2018.12.008.
URL http://www.sciencedirect.com/science/article/pii/S0927025618307870

[37] A. Barua, M. Zhou, A lagrangian framework for analyzing microstructural level response of polymer-bonded explosives, Modelling and Simulation in Materials Science and Engineering 19 (5) (2011) 055001.
URL http://stacks.iop.org/0965-0393/19/i=5/a=055001

[38] X. Wang, Y. Wu, F. Huang, T. Jiao, R. J. Clifton, Mesoscale thermal-mechanical analysis of impacted granular and polymer-bonded explosives, Mechanics of Materials 99 (2016) 68 – 78. doi:https://doi.org/10.1016/j.mechmat.2016.05.004.
URL http://www.sciencedirect.com/science/article/pii/S0167663616300424

[39] D. LaBarbera, M. Zikry, Heterogeneous thermo-mechanical behavior and hot spot formation in rdx–estane energetic aggregates, International Journal of Solids and Structures 62 (2015) 91 – 103. doi:https://doi.org/10.1016/j.ijsolstr.2015.02.007.
URL http://www.sciencedirect.com/science/article/pii/S0020768315000475

[40] W. Yan-Qing, H. Feng-Lei, A micromechanical model for predicting combined damage of particles and interface debonding in pbx explosives, Mechanics of Materials 41 (1) (2009) 27 – 47. doi:https://doi.org/10.1016/j.mechmat.2008.07.005.
URL http://www.sciencedirect.com/science/article/pii/S0167663608001063

[41] A. P. Thompson, H. M. Aktulga, R. Berger, D. S. Bolintineanu, W. M. Brown, P. S. Crozier, P. J. in 't Veld, A. Kohlmeyer, S. G. Moore, T. D. Nguyen, R. Shan, M. J. Stevens, J. Tranchida, C. Trott, S. J. Plimpton, LAMMPS - a flexible simulation tool for particle-based materials modeling at the atomic, meso, and continuum scales, Comput. Phys. Commun. 271 (2022) 108171. doi:10.1016/j.cpc.2021.108171.
URL https://doi.org/10.1016/j.cpc.2021.108171

[42] J. T. Clemmer, M. O. Robbins, Critical Scaling of Solid Fragmentation at Quasistatic and Finite Strain Rates, Phys. Rev. Lett. 129 (7) (2022) 078002. doi:10.1103/PhysRevLett.129.078002.
URL https://doi.org/10.1103/PhysRevLett.129.078002https://link.aps.org/doi/10.1103/PhysRevLett.129.078002

[43] V. D. X. Nguyen, A. K. Tieu, D. André, L. Su, H. Zhu, Discrete element method using cohesive plastic beam for modeling elastoplastic deformation of ductile materials, Comput. Part. Mech. 8 (3) (2021) 437–457. doi:10.1007/s40571-020-00343-4.
URL https://link.springer.com/10.1007/s40571-020-00343-4

[44] A. Lisjak, G. Grasselli, A review of discrete modeling techniques for fracturing processes in discontinuous rock masses, J. Rock Mech. Geotech. Eng. 6 (4) (2014) 301–314. doi:10.1016/j.jrmge.2013.12.007.
URL http://dx.doi.org/10.1016/j.jrmge.2013.12.007https://linkinghub.elsevier.com/retrieve/pii/S1674775514000213

[45] R. D. Groot, P. B. Warren, Dissipative particle dynamics: Bridging the gap between atomistic and mesoscopic simulation, J. Chem. Phys. 107 (11) (1997) 4423–4435. doi:10.1063/1.474784.
URL http://aip.scitation.org/doi/10.1063/1.474784

[46] P. D. Peterson, I. D. J., Microstructural differences between virgin and recycled lots of pbx 9502, Propellants, Explosives, Pyrotechnics 30 (2) (2005) 88 – 94.

[47] C. B. Roth (Ed.), Polymer Glasses, 1st Edition, no. 978-1498711876, CRC Press, 2016.

[48] R. Lakes, Deformation mechanisms in negative Poisson's ratio materials: structural aspects, J. Mater. Sci. 26 (9) (1991) 2287–2292. doi:10.1007/BF01130170.
URL http://link.springer.com/10.1007/BF01130170

[49] A. K. Subramaniyan, C. Sun, Continuum interpretation of virial stress in molecular simulations, Int. J. Solids Struct. 45 (14-15) (2008) 4340–4346. doi:10.1016/j.ijsolstr.2008.03.016.
URL https://linkinghub.elsevier.com/retrieve/pii/S0020768308001248

[50] J. T. Clemmer, I. Srivastava, G. S. Grest, J. B. Lechman, Shear Is Not Always Simple: Rate-Dependent Effects of Flow Type on Granular Rheology, Phys. Rev. Lett. 127 (26) (2021) 268003. arXiv:2107.10085, doi:10.1103/PhysRevLett.127.268003.
URL https://doi.org/10.1103/PhysRevLett.127.268003https://link.aps.org/doi/10.1103/PhysRevLett.127.268003

[51] C. Thornton, L. Zhang, On the evolution of stress and microstructure during general 3D deviatoric straining of granular media, Géotechnique 60 (5) (2010) 333–341. doi:10.1680/geot.2010.60.5.333.
URL http://www.icevirtuallibrary.com/doi/10.1680/geot.2010.60.5.333https://www.icevirtuallibrary.com/doi/10.1680/geot.2010.60.5.333

[52] G. Seidel, D. Allen, K. Helms, S. Groves, A model for predicting the evolution of damage in viscoelastic particle-reinforced composites, Mechanics of Materials 37 (1) (2005) 163 – 178. doi:https://doi.org/10.1016/j.mechmat.2004.01.002.
URL http://www.sciencedirect.com/science/article/pii/S0167663604000092

[53] A. F. Fossum, R. M. Brannon, On a viscoplastic model for rocks with mechanism-dependent characteristic times, Acta Geotech. 1 (2) (2006) 89–106. doi:10.1007/s11440-006-0010-z.
URL http://link.springer.com/10.1007/s11440-006-0010-z

[54] D. C. Drucker, W. Prager, Soil mechanics and plastic analysis or limit design, Q. Appl. Math. 10 (2) (1952) 157–165. doi:10.1090/qam/48291.
URL http://www.ams.org/qam/1952-10-02/S0033-569X-1952-48291-2/

[55] J. Qu, M. Cherkaoui, Fundamentals of micromechanics of solids, Vol. 735, Wiley Online Library, 2006.

[56] T. Kanit, S. Forest, I. Galliet, V. Mounoury, D. Jeulin, Determination of the size of the representative volume element for random composites: statistical and numerical approach, International Journal of Solids and Structures 40 (13) (2003) 3647–3679. doi:https://doi.org/10.1016/S0020-7683(03)00143-4.
URL https://www.sciencedirect.com/science/article/pii/S0020768303001434

[57] D. S. Bolintineanu, R. Waymel, H. Collis, K. N. Long, E. C. Quintana, S. L. Kramer, Anisotropy evolution of elastomeric foams during uniaxial compression measured via in-situ x-ray computed tomography, Materialia 18 (2021) 101112. doi:https://doi.org/10.1016/j.mtla.2021.101112.
URL https://www.sciencedirect.com/science/article/pii/S2589152921001150